Fluid flow and optical flow

TIANSHU LIU[1] AND LIXIN SHEN[2]

[1]Department of Mechanical and Aeronautical Engineering, Western Michigan University,
Kalamazoo, MI 49008, USA
tianshu.liu@wmich.edu

[2]Department of Mathematics, Syracuse University, Syracuse, NY 13244, USA
lshen03@syr.edu

The connection between fluid flow and optical flow is explored in typical flow visualizations to provide a rational foundation for application of the optical flow method to image-based fluid velocity measurements. The projected-motion equations are derived, and the physics-based optical flow equation is given. In general, the optical flow is proportional to the path-averaged velocity of fluid or particles weighted with a relevant field quantity. The variational formulation and the corresponding Euler–Lagrange equation are given for optical flow computation. An error analysis for optical flow computation is provided, which is quantitatively examined by simulations on synthetic grid images. Direct comparisons between the optical flow method and the correlation-based method are made in simulations on synthetic particle images and experiments in a strongly excited turbulent jet.

1. Introduction

Quantitative measurements of velocity fields of flows are of fundamental importance in the studies of fluid mechanics, aerodynamics and thermal/fluid sciences in order to understand the physics of complex flows. Particle image velocimetry (PIV) is a widely used technique based on local spatial correlation between two successive particle images for global measurements of velocity fields (Adrian 1991; Raffel, Willert & Kompenhans 1998). When the particle concentration is sufficiently low that the correspondence between individual particles at successive instants can be identified, particle-tracking velocimetry (PTV) is applicable (Maas, Gruen & Papantoniou 1993; Dracos & Gruen 1998). Without a particular awareness of fluid mechanics problems, computer vision scientists have studied the optical flow problem to analyse the general visual motion in images produced by a moving rigid or quasi-rigid body in the physical world. To determine the visual motion from a time sequence of images, Horn & Schunck (1981) originally suggested the brightness constraint equation for the image intensity and proposed a variational formulation for computing the optical flow. Since then, considerable efforts have been made to solve this equation with various constraints (Barron, Fleet & Beauchemin 1994; Haussecker & Fleet 2001).

The optical flow is defined as the velocity field in the image plane that transforms one image into the next image in a time sequence. In fact, the brightness constraint equation assumes that the image intensity remains invariant along a stream of images. However, the brightness constraint equation is not derived from any physical principle for a physical process, and therefore it does not exactly hold from a physical point of view. More importantly, the optical flow in the brightness constraint equation does not have a clearly defined physical meaning, and as a result it cannot be generally

and directly used for quantitative measurements of physical quantities from images for most scientific and engineering problems.

Nevertheless, from a standpoint of methodology, the optical flow method clearly has a great potential in the determination of high-resolution velocity fields from various images of continuous patterns. Images acquired by optical sensors in various flows in laboratories and nature are the continuous visual representations of some physical quantities such as images of laser-sheet-induced fluorescence, schlieren images of compressible shear layers, images of large-scale cloud motions in planetary atmospheres and infrared images of large-scale motions in oceans. In addition, the variational formulation for optical flow computation can be easily adapted to incorporate suitable physical and geometric constraints into a particular problem. Therefore, it is desirable to explore a rational foundation for application of the optical flow method in fluid mechanics measurements, providing a useful alternative to existing techniques.

Recent effort has been made to apply the optical flow method to flow measurements. Quenot, Pakleza & Kowalewski (1998) proposed the optical flow method with dynamic programming as an alternative to the correlation-based method for PIV images without using a differential equation. Ruhnau *et al.* (2005) and Yuan, Schnorr & Memin (2007) used the brightness constraint equation for PIV images. Realizing that the brightness constraint equation is not an accurate model for fluid measurements, Corpetti, Memin & Perez (2002) and Corpetti *et al.* (2006) proposed the integrated continuity equation in the image plane as an alternative based on the continuity equation of fluid in the three-dimensional object space under some assumptions. The main assumption is that the radiance is proportional to an integral of the fluid density across a measurement domain. This assumption is good only for light transmittance through a fluid with a variable density (Wildes *et al.* 2000; Heas *et al.* 2007), but it is not generally correct for many widely used flow visualizations. Although the integrated continuity equation is currently used in satellite imagery, it is not rigorously derived from the fundamental equations of fluid mechanics for a range of applications, such that its rational foundation for flow measurements has been often questioned (Corpetti *et al.* 2006; Cuzol, Hellier & Memin 2007; Heas *et al.* 2007). Nevertheless, experimental examination of the optical flow method based on the integrated continuity equation for PIV measurements in a mixing layer and a wake behind a circular cylinder has shown a good agreement with hot-wire probe measurements in both the mean velocity profiles and the statistical quantities of turbulence (Corpetti *et al.* 2006). This promising application is fortunately due to the fact that the material derivative in the integrated continuity equation has the same form as that in the physics-based optical flow equation derived in this paper, and the boundary flux terms can be largely neglected for PIV. However, Corpetti *et al.* (2006) did not give a mathematical definition and physical meaning of the optical flow in their equation particularly for PIV. In their earlier work, Corpetti *et al.* (2002) gave a definition of the optical flow as a fluid-density-weighted velocity that is correct only for transmittance images but not for PIV images. Clearly, it is highly desirable to provide a mathematical connection between the optical flow and fluid flow for various flow visualizations, such that application of the optical flow method to global quantitative flow diagnostics can be legitimized.

Interestingly, Su & Dahm (1996*a*, *b*) bypassed the projected motion in the image plane and proposed a variational formulation directly based on the scalar transport equation in the three-dimensional object space to determine three-dimensional velocity fields from laser-induced fluorescence measurements of tempo-spatial scalar

fields. Time-resolved measurements of volumetric scalar fields have been made in practice by using a laser-scanning system and a high-speed photosensitive array (Dahm, Su & Southerland 1992; Frederiksen, Dahm & Dowling 1997). Such measurements are feasible only when a time interval between two successive scan planes is sufficiently small that a three-dimensional data volume reconstructed from a set of data planes can be considered to be frozen in time.

At this stage, the major problem in applying the optical flow method to fluid mechanics measurement is that the connection between the optical flow and fluid flow has not been established quantitatively. Once this problem is solved, the optical flow method that as a differential approach is more appropriate for images of continuous patterns will provide a useful extension complementary to existing techniques like PIV. The objective of this work is to give a direct connection between the optical flow and fluid flow for typical flow visualizations, including laser-sheet-induced fluorescence, transmittance through transported passive scalar, schlieren, shadowgraph and transmittance imaging in density-varying flows, transmittance and scattering of particulate flows and laser-sheet visualization of particles in flows. First, the object-space coordinate frame, perspective projection and image intensity are briefly discussed. Next, the projected-motion equations are derived in Appendix A based on projection of the transport equations or continuity equation in the three-dimensional object space onto the image plane for typical flow visualizations. These equations provide the relationship between the radiance projected to a camera and the path-averaged velocity field weighted with a relevant field quantity. The projected-motion equations for various flow visualizations have a generic mathematical form, and then the physics-based optical flow equation is given. It is clearly indicated that the optical flow is proportional to the path-averaged velocity of fluid or particles. To calculate the optical flow, a variational formulation with a first-order smoothness constraint is given, and the corresponding Euler–Lagrange equation is derived. An error analysis is given to identify and assess the major error sources in optical flow computations, such as the effects of the image intensity gradient and time interval. To quantitatively evaluate the accuracy of the optical flow method and the main results of the error analysis, simulations are conducted on synthetic grid images, where a uniform flow over a vortex pair is imposed. Further simulations focus on application of the optical flow method to particle images and direct comparisons with the correlation-based methods. Finally, velocity measurements in a strongly excited turbulent jet are conducted to compare the optical flow method with the correlation-based method for PIV images. The proposed methodology of projecting relevant governing equations onto the image plane is generally and naturally applicable to other important image-based measurements; for example projection of the thin-oil-film equation for luminescent oil has recently produced quantitative global skin friction diagnostics for complex flows (Liu *et al.* 2008*a*, *b*).

2. Geometric and radiometric projections

The perspective projection from a fluid medium onto an image is illustrated in figure 1. The perspective projection transformation between the three-dimensional object-space coordinates and the image coordinates is usually given by the collinearity equations (McGlone 1998; Faugeras & Luong 2001; Mikhail, Bethel & McGlone 2001; Liu 2004). As shown in figure 1, the orthogonal row vectors ($\boldsymbol{m}_1$, $\boldsymbol{m}_2$, $\boldsymbol{m}_3$) in the rotational matrix in the collinearity conditions constitute a special object-space coordinate frame located at the perspective centre associated with a camera/lens
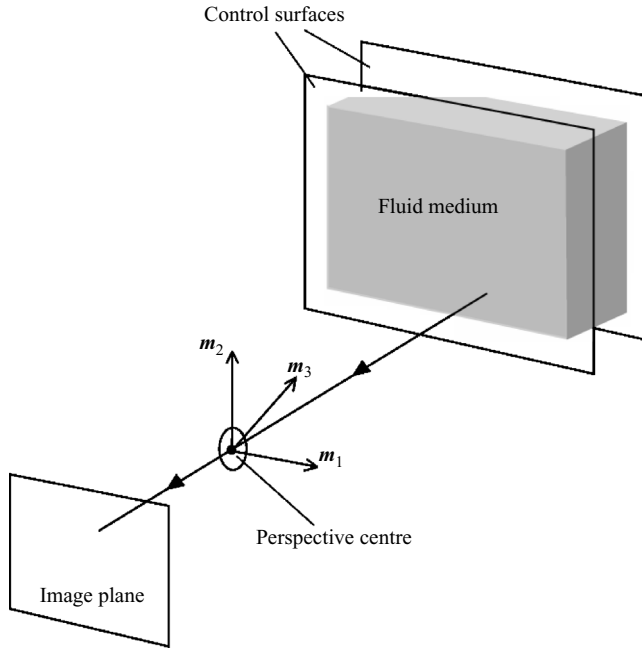
FIGURE 1. Projection from fluid flow onto the image plane.

system. The vectors $\boldsymbol{m}_1$ and $\boldsymbol{m}_2$ are the directional cosine vectors parallel to the x_1-axis and the x_2-axis in the image coordinate system, respectively. The vector $\boldsymbol{m}_3$ is normal to the image plane, directing the object along the optical axis. We denote the object coordinates $\boldsymbol{X} = (X_1, X_2, X_3)$ as the projections of the object-space position vector from the perspective centre in this frame. The perspective projection transformation in this frame is $x_\beta - x_{\beta,p} - \delta x_\beta = \lambda X_\beta$ $(\beta = 1, 2)$, where $\boldsymbol{x} = (x_1, x_2)$ are the image coordinates; the scaling factor $\lambda = -f/X_3$ is a ratio between the principal distance f and the coordinate along $-\boldsymbol{m}_3$; $x_{\beta,p}$ denotes the principal point location in the image plane; and δx_β are the lens distortion terms. The vectors $(\boldsymbol{m}_1, \boldsymbol{m}_2, \boldsymbol{m}_3)$, which are a function of the Euler rotational angles of a camera, can be determined by geometric camera calibration (Tsai 1987; Liu *et al.* 2000; Fraser 2001; Gruen & Huang 2001).

In the object-space frame $(\boldsymbol{m}_1, \boldsymbol{m}_2, \boldsymbol{m}_3)$ associated with a camera, the image intensity is proportional to the radiative flux projected onto the plane (X_1, X_2), i.e.

$$I(\boldsymbol{x}, t) = c \int L(X_1, X_2, t; \theta, \psi) \cos\theta \, \mathrm{d}\Omega, \tag{1}$$

where L is the radiance from an emitting object to an imaging system (e.g. camera), c is a coefficient related to the imaging system, and θ and ψ are the polar angle and azimuthal angle defining the direction of the infinitesimal solid angle $\mathrm{d}\Omega = \sin\theta \, \mathrm{d}\theta \, \mathrm{d}\psi$ of the camera. In fact, integration over a wavelength band is applied in (1), which is not explicitly expressed for brevity. The image coordinates $\boldsymbol{x}$ are related to the object-space coordinates $\boldsymbol{X}$ through the perspective projection transformation.

When a camera is sufficiently far away from an emitting object that the solid angle of the camera is small, the image intensity is $I(\boldsymbol{x}, t) = cL(X_1, X_2, t; \theta_c, \psi_c) \cos\theta_c \Delta\Omega$, where $\Delta\Omega$ is the solid angle of the camera, and the polar angle θ_c and the azimuthal angle ψ_c give the angular position of the camera. In particular, when the radiance is

independent of the azimuthal angle, $I(\boldsymbol{x}, t) = c2\pi L(X_1, X_2, t; \mu_c)\mu_c\Delta\mu_c$, where μ_c is the directional cosine of the camera's polar angle, and $\Delta\mu_c$ is the directional cosine difference of the polar angle defining the observing solid angle of the camera. The scattering from small particles and the emission from luminescent molecules can be considered to be independent of the azimuthal angle. In summary, the image intensity is proportional to the radiance projected onto a camera with a fixed position and viewing direction. Therefore, the relative radiance can be replaced by the relative image intensity in the derivations of the projected-motion equations.

3. Generic projected-motion equation and optical flow equation

The detailed derivations of the projected-motion equations are presented in Appendix A for typical flow visualizations such as laser-sheet-induced fluorescence, transmittance through transported passive scalar, schlieren, shadowgraph and transmittance imaging in density-varying flows, transmittance and scattering of particulate flows and laser-sheet visualization of particles in flows. The projected-motion equations for these different flow visualizations have a form typical of the transport equation. Therefore, we deduce a generic form from these equations:

$$\frac{\partial g}{\partial t} + \nabla_{12} \cdot (g\langle \boldsymbol{U}_{12}\rangle_\psi) = f(X_1, X_2, g), \tag{2}$$

where $g = g(I)$ is a function of the normalized image intensity that is proportional to the radiance received by a camera. The specific forms of $g(I)$ for the flow visualizations are given in Appendix A. In (2), the path-averaged velocity weighted with a field quantity ψ related to a visualizing medium is defined as

$$\langle \boldsymbol{U}_{12}\rangle_\psi = \frac{\displaystyle\int_{\Gamma_1}^{\Gamma_2} \psi \boldsymbol{U}_{12}\, \mathrm{d}X_3}{\displaystyle\int_{\Gamma_1}^{\Gamma_2} \psi\, \mathrm{d}X_3}, \tag{3}$$

where $\boldsymbol{U}_{12} = (U_1, U_2)$ are the projected components onto the coordinate plane (X_1, X_2) of the fluid or particle velocity $\boldsymbol{U} = (U_1, U_2, U_3)$ in the object space frame $(\boldsymbol{m}_1, \boldsymbol{m}_2, \boldsymbol{m}_3)$ associated with a camera. Accordingly, $\nabla_{12} = (\partial/\partial X_1, \partial/\partial X_2)$ in (2) is the gradient operator ∇ projected on the plane (X_1, X_2). As shown in figure 1, the visualized flow domain is confined by two control surfaces, $X_3 = \Gamma_1(X_1, X_2)$ and $X_3 = \Gamma_2(X_1, X_2)$, that could be virtual or solid. In many cases, the planar control surfaces, $X_3 = \Gamma_1 = const.$ and $X_3 = \Gamma_2 = const.$, are used. The field quantity ψ is the scalar concentration in flows (e.g. dye), fluid density in density-varying flows or particle number per unit total volume for particulate flows, as indicated in Appendix A. The introduction of the path-averaged velocity is more than a convenient, unified mathematical treatment for various flow visualizations. For example although researchers in PIV always know that the measured velocity is a certain averaged velocity across a laser sheet, a mathematical definition of the averaged velocity has never been clearly given in a systematical way. A rational definition of the averaged velocity is provided by (3), even though it may be arguable whether the definition is unique. When ψ is approximately constant across a thin laser sheet, $\langle \boldsymbol{U}_{12}\rangle_\psi \approx \boldsymbol{U}_{12}$.

The term $f(X_1, X_2, g)$ in (2) depends on a specific flow visualization technique used in measurements (see Appendix A). For several visualizations like laser-sheet-induced fluorescence images and laser-sheet-illuminated particle images,

$$f(X_1, X_2, g) = D\nabla_{12}^2 g + DcB + c\boldsymbol{n} \cdot (\psi\boldsymbol{U})|_{\Gamma_1}^{\Gamma_2}, \tag{4}$$

where D is the diffusion coefficient; c is a coefficient for fluorescence, scalar absorption or particle scattering/absorption; and $B = -\boldsymbol{n} \cdot \nabla \psi|_{\Gamma_1}^{\Gamma_2} - \nabla_{12} \cdot (\psi|_{\Gamma_2} \nabla_{12} \Gamma_2 + \psi|_{\Gamma_1} \nabla_{12} \Gamma_1)$ is a boundary term that is related to ψ and its derivatives coupled with the derivatives of the control surfaces. The third term on the right-hand side of (4) represents the accumulation effect of the quantity ψ in the volume across the control surfaces. Note that an additional term for the effect of the fluid density variation occurs in (A9) for density-varying flows in Appendix A. These boundary terms for individual techniques are discussed in Appendix A. For the planar control surfaces, all the terms related to the derivatives of the control surfaces vanish. For the solid control surfaces (e.g. glass windows), the zero-flux condition $\boldsymbol{n} \cdot (\psi \boldsymbol{U})|_{\Gamma_1}^{\Gamma_2} = 0$ is imposed. For the virtual control surfaces confining a laser sheet, the term $\boldsymbol{n} \cdot (\psi \boldsymbol{U})|_{\Gamma_1}^{\Gamma_2}$ represents a rate of accumulation of ψ within a laser sheet. In planar PIV measurements, it is often neglected and treated as an error source. In addition, for a laser sheet, the term $\boldsymbol{n} \cdot \nabla \psi|_{\Gamma_1}^{\Gamma_2}$ can be neglected when ψ is constant or linear across the thin laser sheet. Therefore, for laser-sheet visualization, a reasonable approximation is that all the boundary terms can be neglected. For the process of light transmittance through a flow in an open space, the virtual control surfaces can be placed sufficiently far away from the flow that $\boldsymbol{n} \cdot (\psi \boldsymbol{U})|_{\Gamma_1}^{\Gamma_2} = 0$ is satisfied. In the worst scenario in which these boundary terms cannot be either neglected or evaluated, a solution to (2) for $f = 0$ gives, at least, a first-order approximation that may be good enough for some applications, where all the omitted terms must be treated as the elemental error sources in an analysis of results. In this case, although an accurate solution cannot be obtained, (2) still provides a useful framework for a systematical uncertainty analysis because the specific forms of the elemental error sources are given and their effects on optical flow computations can be estimated.

The gradient operator and Laplace operator can be transformed and expressed in the image coordinates by using the perspective projection transformation, i.e. $\partial/\partial X_\beta = \lambda \partial/\partial x_\beta$ and $\partial^2/\partial X_\beta \partial X_\beta = \lambda^2 \partial^2/\partial x_\beta \partial x_\beta$ (where $\beta = 1, 2$). The velocity in the image plane, which is referred as to the optical flow, is $\boldsymbol{u} = (u_1, u_2) = \lambda \langle \boldsymbol{U}_{12} \rangle_\psi$. This relation gives a clear physical meaning of the optical flow; that is the optical flow is proportional to the path-averaged velocity of fluid or particles in flow visualizations. Therefore, (2) can be written as the physics-based optical flow equation

$$\frac{\partial g}{\partial t} + \nabla \cdot (g \boldsymbol{u}) = f(x_1, x_2, g), \tag{5}$$

where $\nabla = \partial/\partial x_\beta$, $f(x_1, x_2, g) = \lambda^2 D \nabla^2 g + Dc B + c \boldsymbol{n} \cdot (\psi \boldsymbol{U})|_{\Gamma_1}^{\Gamma_2}$ and $\nabla^2 = \partial^2/\partial x_\beta \partial x_\beta$. The measured quantity g is also mapped onto the image plane.

It is necessary to compare (5) with the brightness constraint equation $\partial g/\partial t + \boldsymbol{u} \cdot \nabla g = 0$ proposed by Horn & Schunck (1981). Clearly, only for $\nabla \cdot \boldsymbol{u} = 0$ and $f = 0$, (5) has the same form as the Horn–Schunck optical flow equation. For laser sheet visualization in a strictly two-dimensional incompressible flow ($U_3 = 0$), if ψ is constant across the laser sheet, $\nabla_{12} \cdot \langle \boldsymbol{U}_{12} \rangle_\psi = \nabla_{12} \cdot \boldsymbol{U}_{12} = 0$ and then $\nabla \cdot \boldsymbol{u} = 0$. However, in a general case, $\nabla \cdot \boldsymbol{u} \neq 0$ because not only $\nabla_{12} \cdot \langle \boldsymbol{U}_{12} \rangle_\psi \neq \nabla_{12} \cdot \boldsymbol{U}_{12}$ but also $\nabla_{12} \cdot \boldsymbol{U}_{12} = -\partial U_3/\partial X_3 \neq 0$.

4. Variational formulation

To determine the optical flow, a variational formulation with a smoothness constraint has been proposed by Horn & Schunck (1981), which in fact is the first-order form of Tikhonov's formulation for ill-posed problems (Tikhonov & Arsenin

1977). Corpetti *et al.* (2006) discussed the shortcomings of the first-order regularization in flow measurements and suggested a regularization functional based on the gradients of divergence and curl to preserve the spatial characteristics of divergence and vorticity in flows. Use of this second-order div–curl (divergence and curl) regularization is more plausible conceptually to preserve fine structures in turbulent flows. However, the existing forms of regularization are not derived on the basis of the principles of fluid mechanics. To develop physics-based constraints, a rational approach would be to project the Navier–Stokes equations onto the image plane to provide a constraint for optical flow computation. This will lead to a complicated, nonlinear constraint that is worth further investigation. Here, the Horn–Schunck constraint is used mainly due to its simplicity.

Given g and f, we define a functional

$$J(\boldsymbol{u}) = \int_A [\partial g/\partial t + \nabla \cdot (g\boldsymbol{u}) - f]^2 \, \mathrm{d}x_1 \, \mathrm{d}x_2 + \alpha \int_A (|\nabla u_1|^2 + |\nabla u_2|^2) \, \mathrm{d}x_1 \, \mathrm{d}x_2, \quad (6)$$

where α is the Lagrange multiplier. To minimize $J(\boldsymbol{u})$, we introduce an arbitrary smooth function $\boldsymbol{v} = (v_1, v_2)$, compute $\mathrm{d}J(\boldsymbol{u} + p\boldsymbol{v})/\mathrm{d}p|_{p=0}$, and using the Green theorem where the Neumann condition $\partial \boldsymbol{u}/\partial n = 0$ is imposed on the image domain boundary ∂A we obtain the Euler–Lagrange equation

$$g\nabla[\partial g/\partial t + \nabla \cdot (g\boldsymbol{u}) - f] + \alpha \nabla^2 \boldsymbol{u} = 0. \quad (7)$$

Surprisingly, for $\nabla \cdot \boldsymbol{u} = 0$ and $f = 0$, (7) does not directly reduce to the Euler–Lagrange equation given by Horn & Schunck (1981). To examine a connection with the original variational formulation given by Horn & Schunck (1981), integrating (7) along a closed contour C in the image plane yields

$$\oint_C (g\nabla[g_t + \nabla \cdot (g\boldsymbol{u}) - f] + \alpha \nabla^2 \boldsymbol{u}) \cdot \mathrm{d}\boldsymbol{r} = 0,$$

and further

$$\oint_C (-[g_t + \nabla \cdot (g\boldsymbol{u}) - f]\nabla g + \alpha \nabla^2 \boldsymbol{u}) \cdot \mathrm{d}\boldsymbol{r} = 0. \quad (8)$$

Since the contour C is arbitrary, for $\nabla \cdot \boldsymbol{u} = 0$ and $f = 0$, (8) recovers the Euler–Lagrange equation $[g_t + \boldsymbol{u} \cdot \nabla g]\nabla g - \alpha \nabla^2 \boldsymbol{u} = 0$ originally given by Horn & Schunck (1981); but this reduction is not particularly straightforward.

A mathematical analysis of the variational formulation of the brightness constraint equation has been given by Aubert, Deriche & Kornprobst (1999) and Weickert & Schnorr (2001), and the convergence of the numerical solution of the corresponding Euler–Lagrange equation has been proven by Mitiche & Mansouri (2004). However, (5), the physics-based optical flow equation, and (7), the corresponding Euler–Lagrange equation, are the generalized forms of those given by Horn & Schunck (1981). Although an analysis of the functional formulation and numerical solution of (7) is extremely worthwhile for further investigation, this non-trivial mathematical problem is not within the scope of this paper. A discrete form of (7) is given in Appendix B, and the linear system is solved by using Jacobi's blockwise iteration. The solution of Horn & Schunck's equation is used as an initial approximation for (7) for faster convergence. Note that a variational formulation with the same first-order smoothness constraint was given by Su & Dahm (1996a, b) directly for the scalar transport equation in the three-dimensional object space to determine three-dimensional velocity fields when time-resolved three-dimensional scalar fields are given. For typical flow visualizations in which the geometric and

radiometric projections cannot be bypassed, however, the variational problem should be formulated in the image plane based on the physics-based optical flow equation.

5. Error analysis

In order to examine the error propagation, the image intensity and optical flow are decomposed into a basic solution and an error, i.e. $g = g_o + \Delta g$ and $\boldsymbol{u} = \boldsymbol{u}_o + \Delta \boldsymbol{u}$, where g_o and $\boldsymbol{u}_o$ exactly satisfy (7), the Euler–Lagrange equation; $\Delta \boldsymbol{u}$ is the resulting error in the optical flow; and Δg is a variation or difference in the image intensity in measurements and numerical calculations. Substituting $g = g_o + \Delta g$ and $\boldsymbol{u} = \boldsymbol{u}_o + \Delta \boldsymbol{u}$ into (7), neglecting small terms of higher order and assuming that the difference and differential operators are exchangeable, we obtain an error propagation equation:

$$g\nabla[D_g + \nabla g \cdot (\Delta \boldsymbol{u})] + \alpha \nabla^2(\Delta \boldsymbol{u}) = \alpha(\Delta g/g)\nabla^2 \boldsymbol{u}, \tag{9}$$

where

$$D_g = \Delta(\partial g/\partial t) + \Delta(\nabla g) \cdot \boldsymbol{u} + g\Delta(\nabla \cdot \boldsymbol{u}) + \Delta g(\nabla \cdot \boldsymbol{u}). \tag{10}$$

The first and second terms in (10) are the numerical errors in calculating the temporal and spatial derivatives of the image intensity, respectively. The third and fourth terms are the variation in the divergence of the optical flow and the variation of the image intensity, respectively. The right-hand term in (9) is an error associated with the image intensity change in the regularization.

The elemental error sources in (9) are $\Delta(\partial g/\partial t)$, $\Delta(\nabla g)$, $\Delta(\nabla \cdot \boldsymbol{u})$ and Δg. Furthermore, the resulting error in the optical flow depends on the image intensity gradient ∇g and the Lagrange multiplier α. To study how the elemental errors affect $\Delta \boldsymbol{u}$ for images that have the same intensity pattern but different intensity gradient, (9) is normalized by a characteristic intensity gradient magnitude $\|\nabla g\|_{char}$ such that the normalized intensity gradient $\|\nabla g\|_{char}^{-1} \nabla g$ largely remains the same in these images. The norm, $\|\nabla g\|_{char}$, can be suitably defined depending on a specific application. Therefore, (9) becomes

$$g\nabla\left[\|\nabla g\|_{char}^{-1} D_g + \|\nabla g\|_{char}^{-1} \nabla g \cdot (\Delta \boldsymbol{u})\right] + \alpha \|\nabla g\|_{char}^{-1} \nabla^2(\Delta \boldsymbol{u}) = \alpha \|\nabla g\|_{char}^{-1} (\Delta g/g)\nabla^2 \boldsymbol{u}. \tag{11}$$

For a limiting case where the elemental errors $\Delta(\nabla g)$, $\Delta(\nabla \cdot \boldsymbol{u})$ and Δg vanish, the optical flow error $\Delta \boldsymbol{u}$ is mainly produced by $\Delta(\partial g/\partial t)$. For the first-order time difference, an estimate is $\Delta(\partial g/\partial t) \cong -g_{tt}\Delta t/2$, where $g_{tt} = \partial^2 g/\partial t^2$ and Δt is a time interval between two consecutive images. In this case, (11) can be written as

$$g\nabla\left[-\|\nabla g\|_{char}^{-1} \Delta t g_{tt}/2 + \|\nabla g\|_{char}^{-1} \nabla g \cdot (\Delta \boldsymbol{u})\right] + \alpha \|\nabla g\|_{char}^{-1} \nabla^2(\Delta \boldsymbol{u}) = 0. \tag{12}$$

The term $\|\nabla g\|_{char}^{-1} \Delta t g_{tt}$ that represents an elemental error in the time differentiation is particularly interesting. Since Δt cannot be zero and $\|\nabla g\|_{char}$ cannot be infinitely large, $\|\nabla g\|_{char}^{-1} \Delta t$ must be finite, i.e.

$$\Delta t \|\nabla g\|_{char}^{-1} = \delta, \tag{13}$$

where δ is a small positive constant. Hence, according to (13), a finite optical flow error, $\Delta \boldsymbol{u}$, always exists, which imposes an ultimate limit in optical flow computation. Based on (13), for a given value of Δt, a larger intensity gradient leads to a smaller error in the optical flow. For images with a large intensity gradient, the requirement for a small Δt is less stringent. In contrast, for images with a smaller intensity gradient magnitude, a sufficiently small Δt is required to achieve a reasonable accuracy. The

consequences drawn from the error analysis will be quantitatively examined through simulations in §6.

6. Simulations: flow over a vortex pair

In order to examine the algorithm and the error analysis, simulations are conducted on synthetic grid images (480×640 pixels and 8 bits), where the intensity profile across a grid line is Gaussian. The grid images simulate grid images tagged by laser-induced-fluorescence for velocity measurements (Koochesfahani & Nocera 2007). An optical flow field, which is generated by superposing an Oseen vortex pair and a uniform flow, is imposed in the images. The two Oseen vortices are placed at $(m/3, n/2)$ and $(2m/3, n/2)$ in an image, respectively, where m (480) and n (640) are the numbers of rows and columns of the image. The circumferential velocity of an Oseen vortex is given by $u_\theta = (\Gamma/2\pi r)[1 - \exp(-r^2/r_0^2)]$, where the vortex strengths are $\Gamma = \pm 7000$ (pixel)^2 s^{-1}, and the vortex core radius is $r_0 = 15$ pixels. The uniform flow velocity is 10 pixels s^{-1}. The grid image deformed by the velocity field after a time step Δt is generated using a discretized form of the optical flow equation (5) for $f(x_1, x_2, g) = 0$. Figure 2(a) shows a 40×40 grid image. A deformed image at $\Delta t = 0.02$ s is generated where the maximum displacement is about 1 pixel. Figure 3 shows the velocity vectors and streamlines extracted from a pair of the grid images. The Lagrange multipliers are 50 for the Horn–Schunck estimator as an initial estimation and 400 for the present method. The Lagrange multiplier within a range of 200–2000 does not affect the velocity profile except near the peak velocity. The extracted velocity profiles across the vortex cores are shown in figure 4. The present method underestimates the maximum velocity just outside the vortex cores, and the Horn–Schunck solution is considerably lower in the outer region. Also, the Horn–Schunck solution exhibits a small spatial variation that corresponds to the grid intensity gradient pattern for the selected Lagrange multiplier of 50. When the Lagrange multiplier is larger, the variation will be smoothed out. Since the Horn–Schunck solution is used as an initial approximation, the selection of the Lagrange multiplier for the Horn–Schunck estimator is not particularly critical here. Figure 5 is a map of the local error of the x-component of velocity defined as $|u_1(i, j) - u_{1,exa}(i, j)|$, where the subscript 'exa' denotes the exact velocity distribution. It is indicated that larger errors in the optical flow occur around the vortex cores, particularly outside the vortex pair. The effect of the grid pattern is visible. It is found that this map approximately corresponds to a map of the elemental error $\Delta(\partial g/\partial t) \cong -g_{tt}\Delta t/2$, where $g_{tt} \cong -\partial/\partial t[\nabla \cdot (g\boldsymbol{u})]$ according to the optical flow equation.

To examine the effect of the intensity gradient magnitude of the grid pattern on the total optical flow error, six grid images shown in figure 2 are generated by changing the standard deviation of the Gaussian intensity distribution of a grid line. Here, the characteristic intensity gradient magnitude in a grid image ($m = 480$, $n = 640$) is defined as

$$\|\nabla g\|_{char} = n^{-1} \sum_{j=1}^{n} \max_{i \in [1, m-1]} |g(i+1, j) - g(i, j)|.$$

The characteristic intensity gradient magnitudes of these grid images are 27.3, 20, 16, 13, 7.8 and 6.5 counts/pixel, respectively. As indicated in figure 6, for both the present method and the Horn–Schunck estimator, the total optical flow errors $\|u_1 - u_{1,exa}\|$ and $\|u_2 - u_{2,exa}\|$ decrease and approach a constant as the intensity gradient magnitude $\|\nabla g\|_{char}$ increases for $\Delta t = 0.02$, where $\|u_k - u_{k,exa}\| = m^{-1}n^{-1}\sum_{i=1}^{m}\sum_{j=1}^{n}|u_k(i, j) - u_{k,exa}(i, j)|$. This is consistent with the error analysis. The
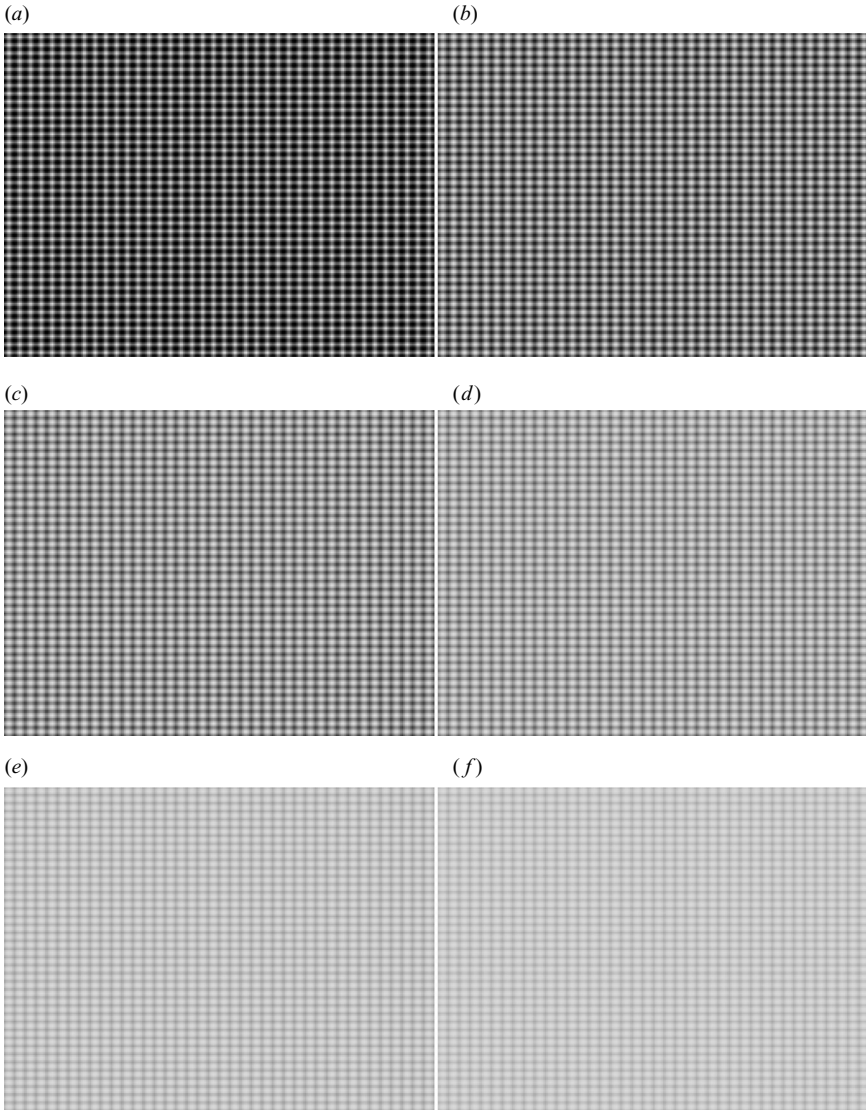
FIGURE 2. Grid images with different characteristic intensity gradient magnitudes: (*a*) 27.3; (*b*) 20; (*c*) 16; (*d*) 13; (*e*) 7.8; and (*f*) 6.5 counts/pixel.

present method has a smaller optical flow error than the Horn–Schunck estimator for a sufficiently large intensity gradient magnitude. As the gradient magnitude decreases, the present method and the Horn–Schunck estimator approach the same error. Figure 7 shows how the intensity gradient magnitude affects the extracted *x*-component velocity profile across the vortex cores. In general, for an image with a small intensity gradient magnitude, the optical flow method tends to underestimate the velocity.

Furthermore, the error analysis indicates that the optical flow error increases with the time interval between two consecutive images. Figure 8 indicates that the total optical flow errors $\|u_1 - u_{1,exa}\|$ and $\|u_2 - u_{2,exa}\|$ increase as the time interval Δt increases for $\|\nabla g\|_{char} = 20$. There is an optimum Δt at which the total optical

(a)

(b)
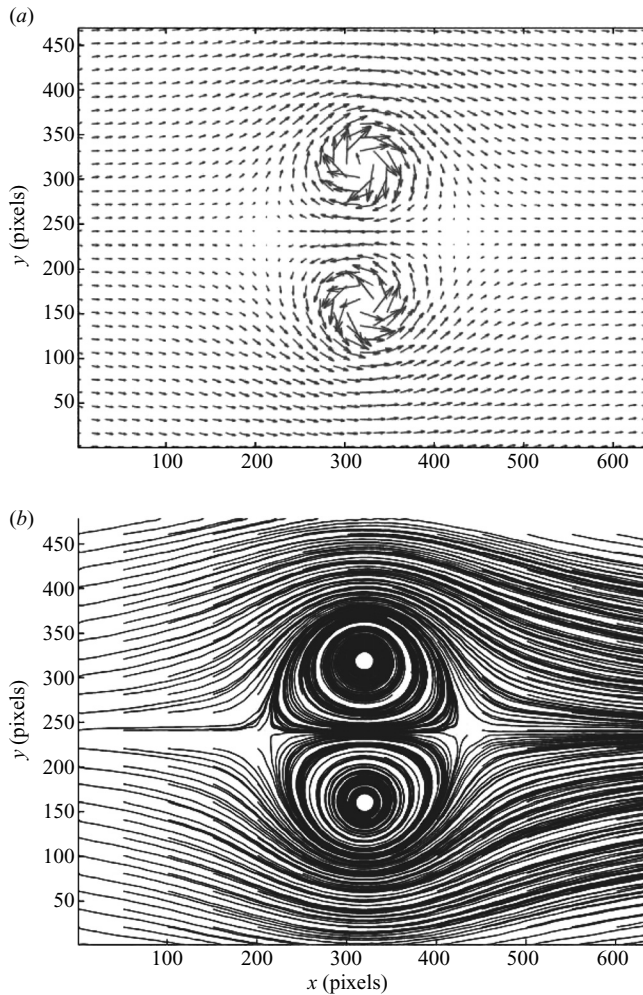
FIGURE 3. (*a*) Velocity vectors and (*b*) streamlines extracted from the grid images (figure 2*a*).

flow error is minimized, which is about 0.01 s, and the corresponding maximum displacement is about 0.5 pixels. For $\Delta t < 0.01$ s, the error is increased particularly near the saddle points, where the velocity is small. The effect of Δt on the extracted x-component velocity profile across the two vortex cores is shown in figure 9. The total optical flow error depends on both $\|\nabla g\|_{char}$ and Δt. When a combined variable $\|\nabla g\|_{char}^{-1}\Delta t$ is used, it is found that all the error data for $\Delta t = 0.01 - 0.1$ s and $\|\nabla g\|_{char} = 6.5 - 27.3$ counts/pixel are roughly collapsed, as shown in figure 10, and the error increases with $\|\nabla g\|_{char}^{-1}\Delta t$ in an approximately linear fashion within these ranges, which is an observation consistent with the error analysis.

Ideally, the synthetic optical flow based on the Oseen vortices and uniform flow satisfies the divergence-free condition ($\nabla \cdot u = 0$), and therefore the present method and the Horn–Schunck estimator should produce the same results. However, the computations just described show that the Horn–Schunck estimator has a larger error. In this simulation, it is found that the first-order spatial difference approximation used in generating the deformed grid images produces an artificial finite divergence of the optical flow ($\nabla \cdot u \neq 0$) embedded in the images around the viscous cores of the
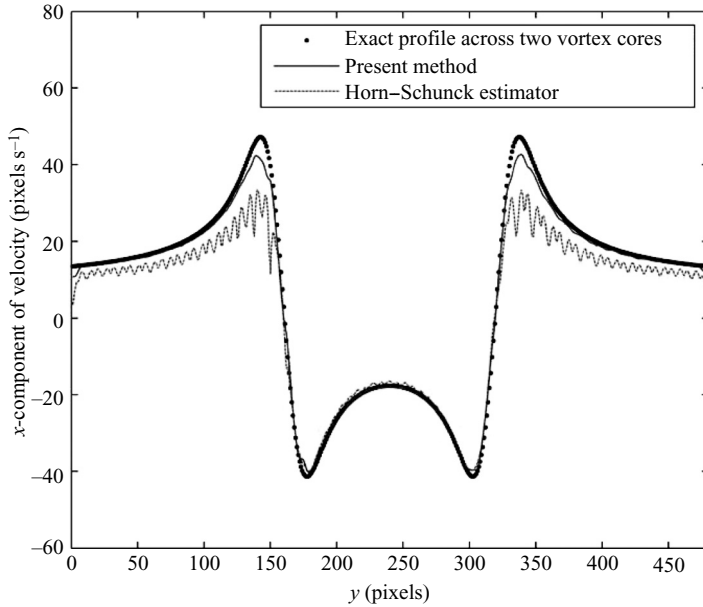
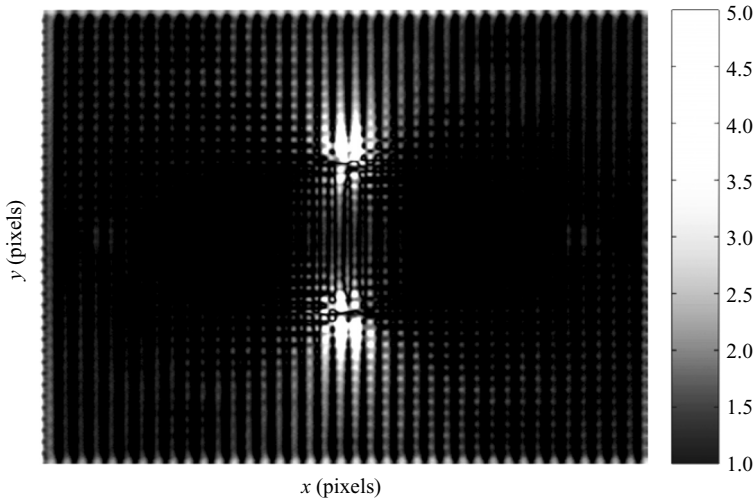FIGURE 4. Distribution of the x-component of velocity across the vortex cores extracted from the grid images.

FIGURE 5. Map of the local optical flow error from the grid images.

Oseen vortices. The Horn–Schunck estimator that imposes $\nabla \cdot \boldsymbol{u} = 0$ does not take into account this finite divergence associated with the numerical approximation, and as a result it has a larger error in these regions.

The error analysis and simulations indicate that a greater error occurs in optical flow computation, particularly in the regions where the velocity has a large change for images with a lower image intensity gradient. To improve the accuracy of optical flow computation, the intensity gradient in images can simply be enhanced by rescaling the images. For example, the grid image (f) in figure 2 is rescaled simply by $5[g - 0.98 \min(g)]$, and the intensity gradient magnitude $\|\nabla g\|_{char}$ is increased from
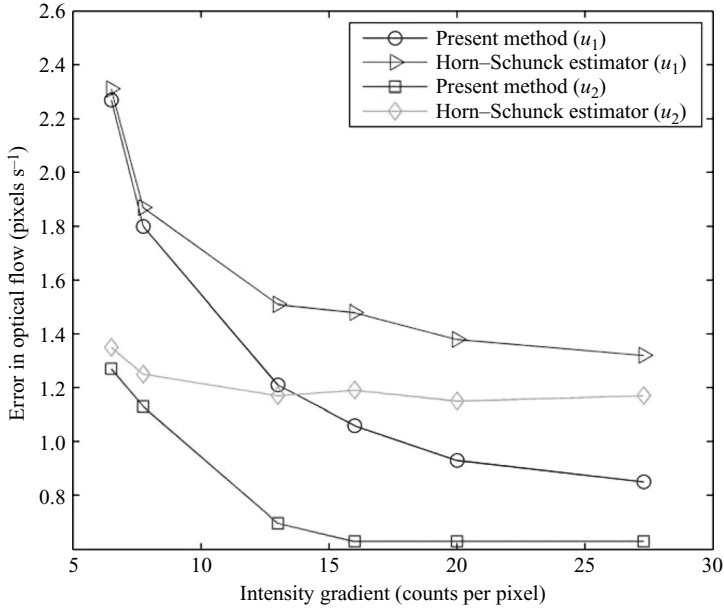
FIGURE 6. Decrease of the total optical flow error on increasing the characteristic intensity gradients in images.
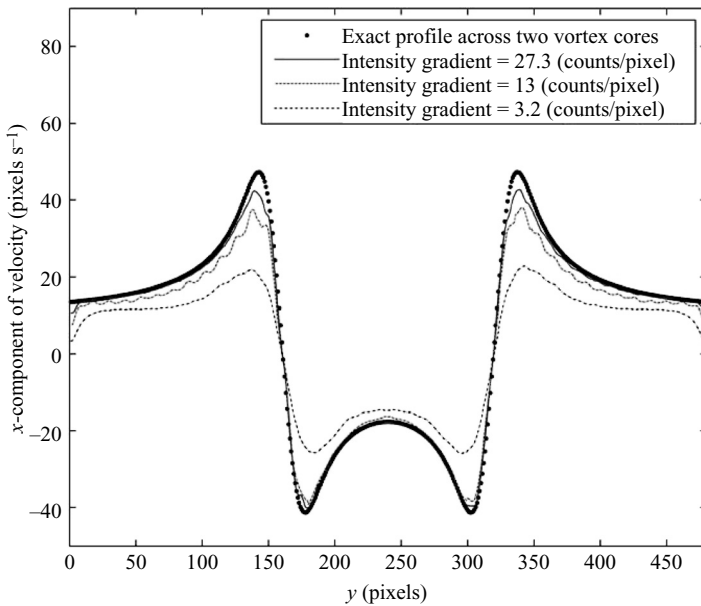

FIGURE 7. Effect of the characteristic intensity gradient on a velocity profile extracted from the grid images.

6.5 to 32.5. As a result, the total optical flow error $\|u_1 - u_{1,exa}\|$ is reduced from 2.3 pixels s^{-1} to 1.7 pixels s^{-1}.
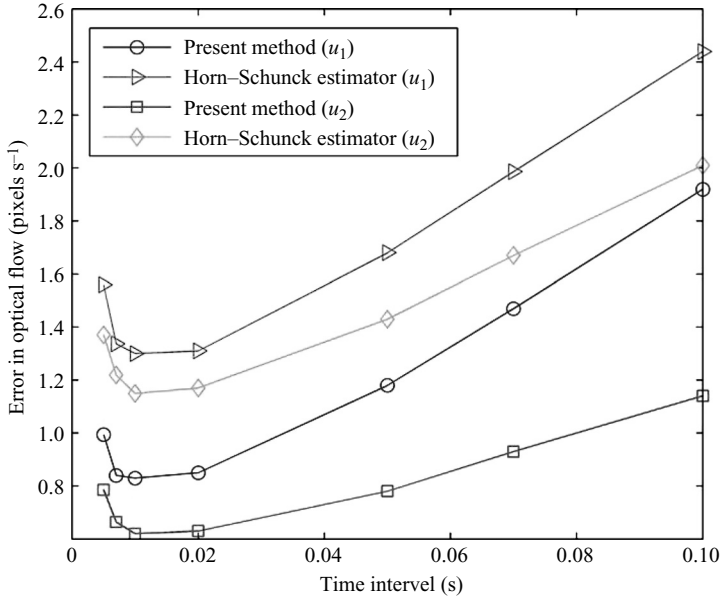
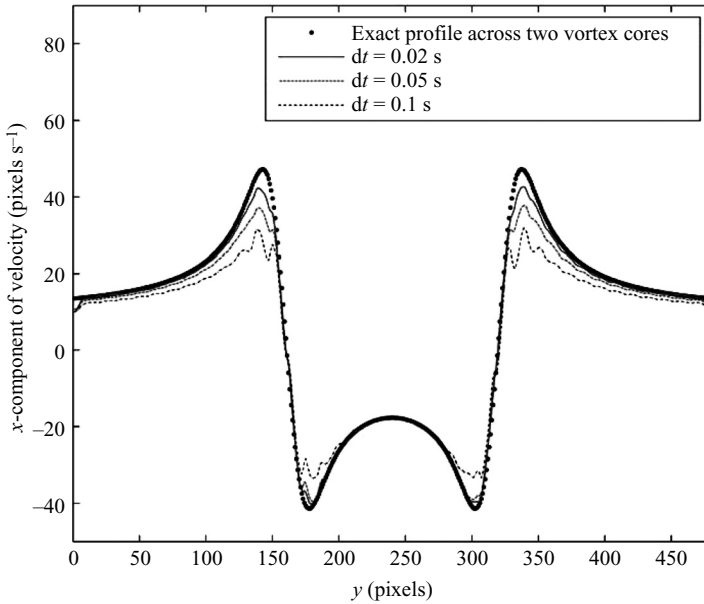FIGURE 8. Effect of the time interval on the total optical flow error for the grid images.

FIGURE 9. Effect of the time interval on a velocity profile extracted from the grid images.

7. Problems for particle images

One question is whether the optical flow method is practically applicable to particle images using the projected-motion equation for laser-sheet-illuminated particle images given in Appendix A, §A.6. Particle images are often utilized in PIV measurements in which particles are displaced between two consecutive images after a time step. When
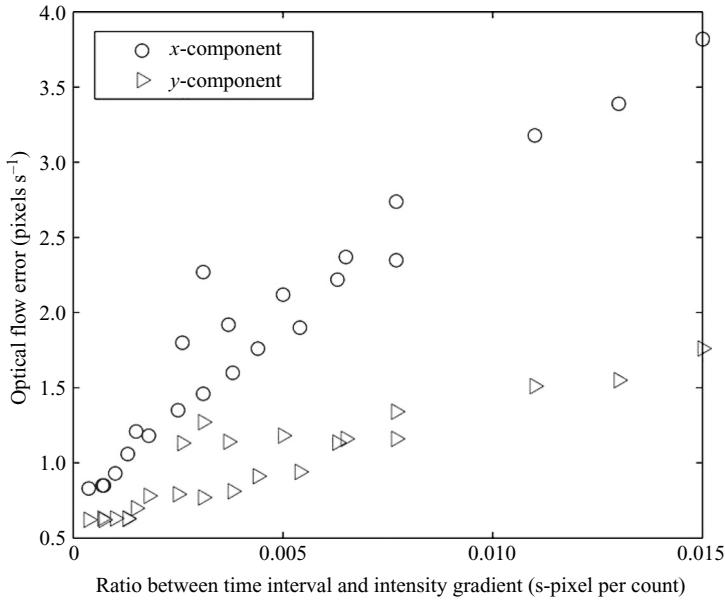
FIGURE 10. The total optical flow error as a function of $\|\nabla g\|_{char}^{-1} \Delta t$.

the displacements are so large that the corresponding particles in the two images are totally separated, the optical flow method fails, since the time derivative $\partial g/\partial t$ cannot be accurately calculated. In this case, the correlation-based method is more effective and accurate for large displacements. In contrast, the optical flow method requires such a small Δt that the corresponding particles in the two consecutive images remain in contact, and therefore $\partial g/\partial t$ can be calculated. To cope with large displacements in PIV images, Corpetti *et al.* (2002, 2006) suggested application of an integrated form of the optical flow equation over a time step rather than a differential form in a variational formulation. Furthermore, a multi-resolution scheme based on a dyadic image pyramid generated using a Gaussian filter was proposed by Ruhnau *et al.* (2005) to successively reconstruct image motions from coarse scales to fine scales for large displacements. Heas *et al.* (2007) combined an image correlation method for large displacements and a variational optical flow method for refined and dense estimation of displacements. This paper strictly focuses on (7), the generic differential form of the Euler–Lagrange equation.

To examine the problems in application of the optical flow method for particle images, low-density images with distinctly discrete particles and high-density particle images are considered. Figure 11 shows an image with a relatively low density and the corresponding Gaussian-filtered image. A velocity field of an Oseen-vortex pair and a uniform flow is imposed in the images. For $\Delta t = 0.02$ s, the maximum displacement is about 1 pixel. This displacement is still visible but much smaller than that in typical PIV images. Even for these images, direct application of the optical flow algorithm does not converge to a solution, since some particles are still too separated. To resolve this problem, a Gaussian filter is applied to the particle images before using the optical flow algorithm. As shown in figure 11(*b*), suitable Gaussian smoothing makes the distinct particles isotropically diffused and the separated particles connected, whereas the displacements remain unchanged. A more diffused image is obtained by applying a Gaussian filter (15×15 pixels mask size and 6 pixels standard deviation) to an
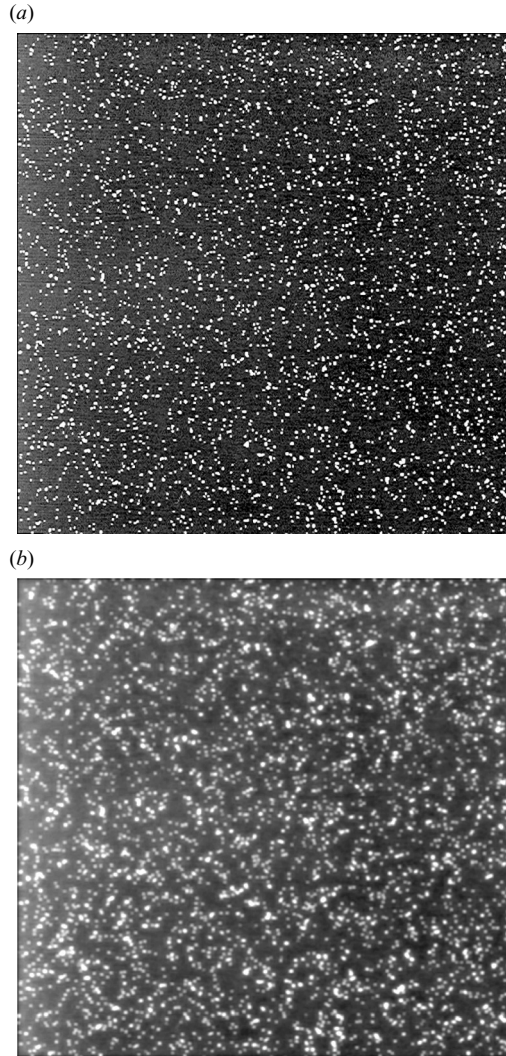
(*a*)

(*b*)

FIGURE 11. (*a*) Image with distinct particles and (*b*) filtered particle image.

original particle image, while another less diffused image is similarly generated by a Gaussian filter (5×5 pixels mask size and 2 pixels standard deviation). The average of the two diffused images gives a composite filtered particle image in figure 11(*b*). Application of the optical flow algorithm to the filtered images leads to a converged solution. Figure 12 shows the velocity vectors and streamlines extracted from the diffused particle images for $\Delta t = 0.02$ s. A map of the local error of the *x*-component of the optical flow is shown in figure 13, which is similar to that for the grid images. The velocity profiles across the two vortex cores for three time intervals are shown in figure 14. The extracted profile is closer to the exact profile for $\Delta t = 0.005$ s. However, it is found that as Δt decreases further the optical flow error actually increases, which is consistent with the simulation for the grid images. It is interesting to see how well the correlation-based method works for the non-filtered particle images shown in figure 11(*a*). The velocity profiles across the two vortex cores are shown in figure 15, and are extracted from the non-filtered particle images using the TSI
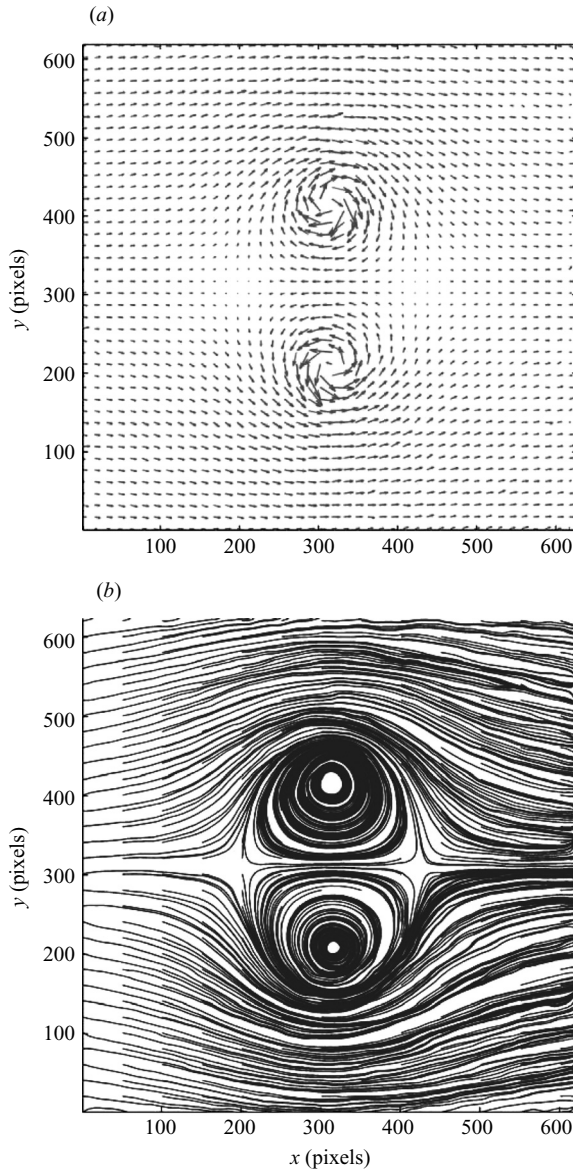
(*a*)

(*b*)

FIGURE 12. (*a*) Velocity vectors and (*b*) streamlines extracted from the filtered particle images.

Insight5 PIV software (64×64 pixels window size). The velocity magnitudes given by all the correlation algorithms are considerably smaller, which is not unexpected, since the particle images with displacements less than 1 pixel are not suitable for correlation-based methods. In addition, interrogation windows of 64×64 pixels tend to smooth out the sharp velocity change near the vortex cores.

High-density particle images, as shown in figure 16, are used for an additional test. These images can be considered as images of almost continuous random patterns with strong spike noise. Again, direct application of the optical flow algorithm to these high-density images fails due to the spatial spike noise. The Gaussian smoothing (5×5 pixels mask size and 2 pixels standard deviation) generates filtered particle
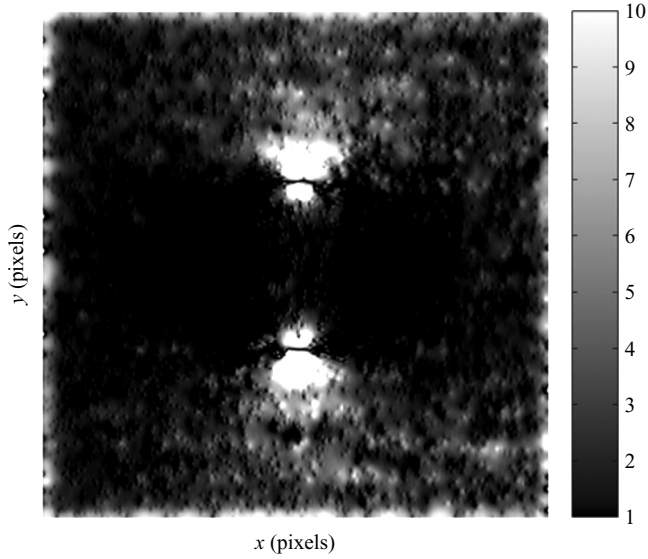
FIGURE 13. Map of the local optical flow error from the filtered particle images.
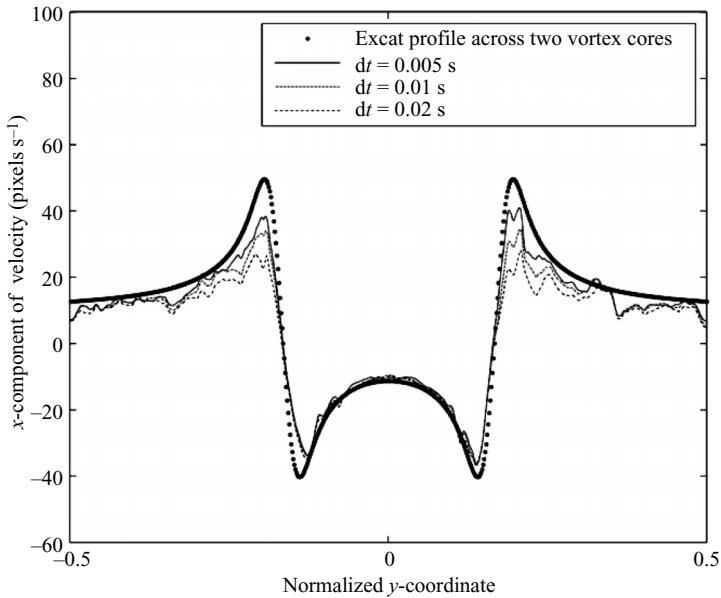

FIGURE 14. Velocity profiles extracted from the filtered particle images for different time intervals.

images to remove high-frequency components, as shown in figure 16(*b*). The velocity profiles across the two vortex cores extracted from the filtered high-density particle images are shown in figure 17 for three time intervals. Although the extracted profiles are consistent with the exact profile, there is a considerable systematical error that is only slightly decreased for a smaller Δt. This systematical error is mainly caused by a relatively small intensity gradient that is further reduced by the Gaussian smoothing. Clearly, there is a tradeoff between the Gaussian smoothing for obtaining a converged
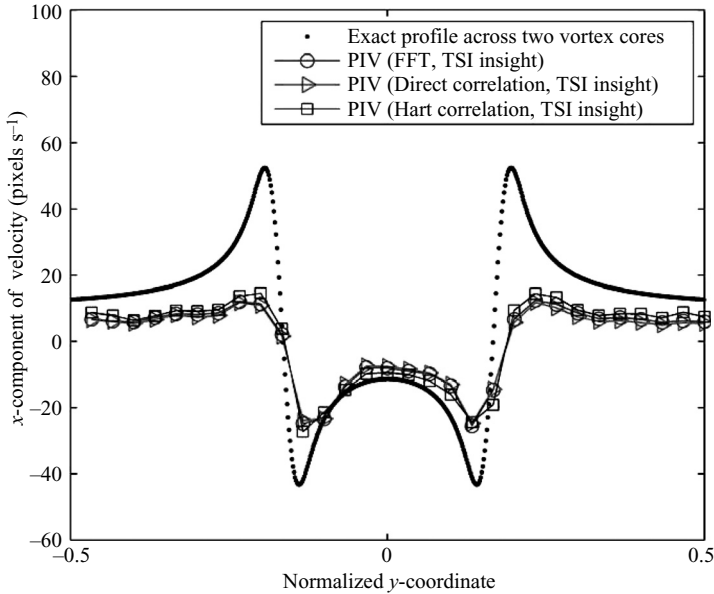
FIGURE 15. Velocity profiles extracted from the non-filtered particle images using the TSI Insight5 PIV software for a time interval of 0.02 s.

solution and the error associated with the reduction of the intensity gradient due to the smoothing. As indicated in figure 18, the correlation-based methods perform poorly not only because the displacements are so small (less than 1 pixel) but also because these images are almost continuous.

The above experiments indicate that the optical flow method is applicable to suitably filtered particle images when Δt is sufficiently small that $\partial g/\partial t$ can be accurately calculated. However, the Gaussian smoothing leads to a reduction of the local intensity gradient and therefore an increase of the optical flow error. The optical flow method prefers images with small displacements and images of nearly continuous patterns for which the correlation-based method is not accurate. However, direct application of the optical flow method without using additional procedures like a multi-resolution scheme (Ruhnau *et al.* 2005) may fail in the case in which particles in two consecutive images have large displacements. In this case, a combination of the correlation-based method and the optical flow method may be more promising.

The Gaussian filtering is used in PIV images before applying the optical flow algorithm to diffuse distinct particles isotropically and make the corresponding particles connected in a pair of images. In addition, Gaussian filtering is required to remove some high-frequency noise in PIV images. Here an assumption is that the Gaussian filtering does not change motion information contained in these images. After the Gaussian filtering, an image g is decomposed into two parts, i.e. $g = A(g) + \Delta g$, where $A(g)$ is a filtered image, and Δg is the remaining part. From the filtered image $A(g)$, the optical flow $\boldsymbol{u}$ is determined. Similarly, the remaining optical flow $\Delta\boldsymbol{u}$ can be obtained from the image Δg, which in a certain sense represents the level of noise in optical flow computation. For dealing with large displacements, the Gaussian filtering and sub-sampling operations have been recursively applied by Ruhnau *et al.* (2005) to construct an image pyramid. A coarse optical flow field is obtained, using the optical flow method, from low spatial frequency images. Then
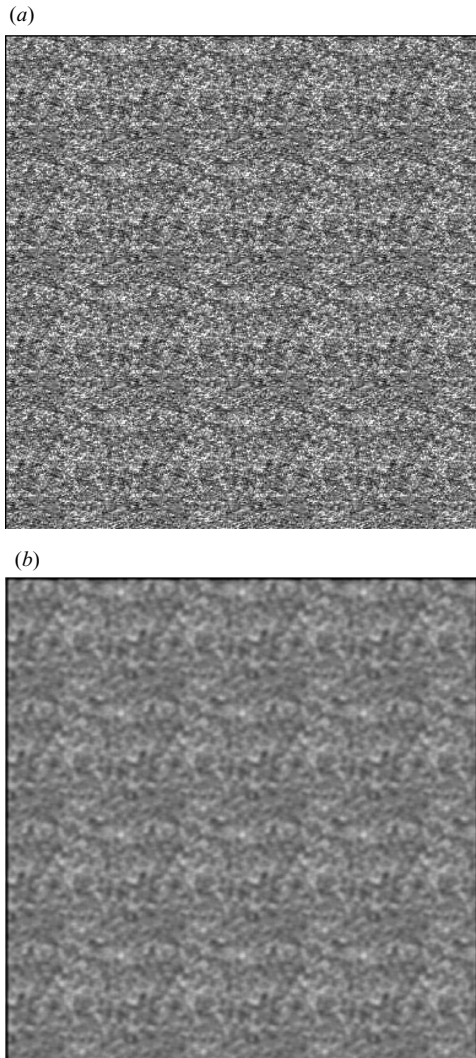
(*a*)

(*b*)

FIGURE 16. (*a*) High-density particle image and (*b*) filtered high-density particle image.

a correction scheme based on the previous optical flow yields a refined optical flow estimation. This multi-resolution process is repeated at scales that keep getting finer until the original image resolution is recovered.

8. Velocity measurements in a strongly excited turbulent jet

In order to experimentally examine the optical flow method, measurements of velocity fields in a strongly excited turbulent jet were conducted by using a PIV system (TSI), in which the density of seeded particles was suitably high for both the optical flow method and the correlation method. Although PIV images are not the best choice for demonstrating the potential capability of the optical flow method, as pointed out before, PIV is the maturest global velocimetry available for one-to-one comparisons with the optical flow method. Figure 19 is a diagram of a jet facility. The facility consists of an oil particle generator (atomizer) and two pressure chambers. Air
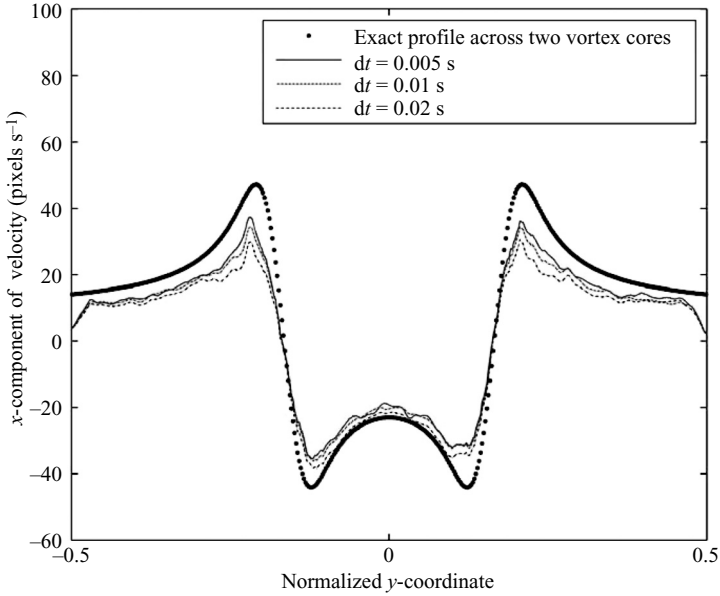
FIGURE 17. Velocity profiles extracted from the filtered high-density particle images for different time intervals.
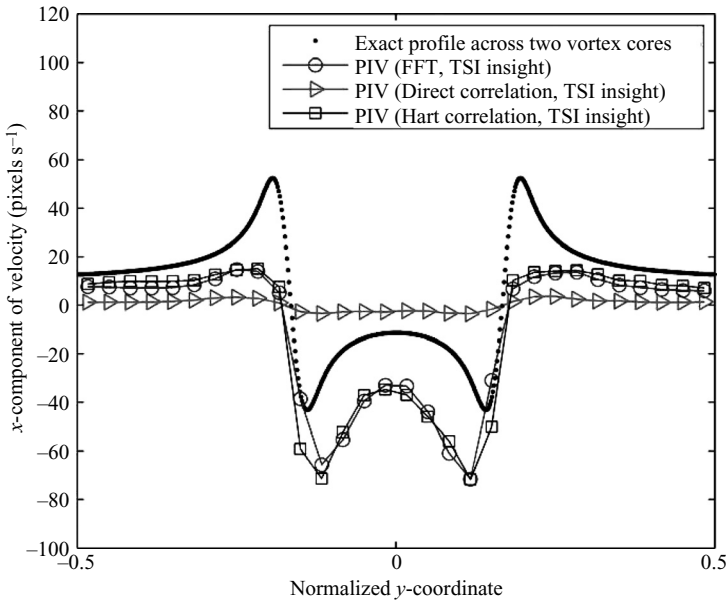
FIGURE 18. Velocity profiles extracted from the original, non-filtered high-density particle images, using the TSI Insight5 PIV software for a time interval of 0.02 s.

from a compressed air line (160 p.s.i.) enters a TSI Model 9307 oil particle generator at a regulated air pressure. Olive oil droplets generated from the atomizer have a distribution with a mean diameter of about 1 micron. Leaving the atomizer, the oil-seeded airflow moves into the first pressure chamber (mixing chamber) through a 3/8 in. clear vinyl tube, where it is then mixed with regulated compressed air. Adding

FIGURE 19. Jet and PIV setup.

regulated compressed air allows the jet velocity to be controlled by changing the pressure inside the mixing chamber. The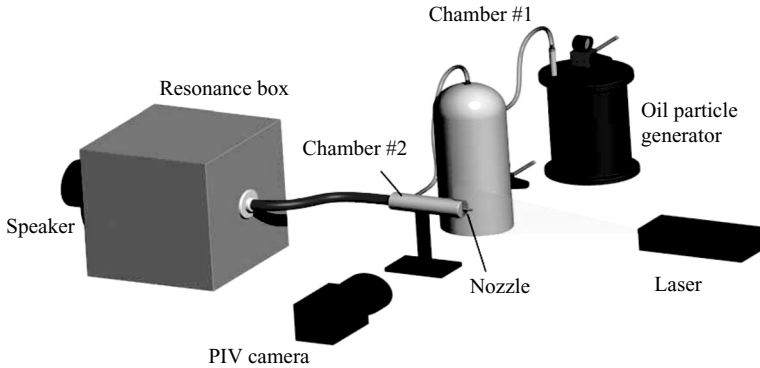 mixing chamber is a 445 mm long capped tube with a 100 mm diameter. The mixed flow exits the top of the mixing chamber and enters the top of the second pressure chamber traveling through a 3/8-in. clear vinyl tube.

Oil film creation inside the pressure chambers and the connecting vinyl tubing often lead to oil pooling, and once a critical point is reached, a large droplet detaches and is swept along the flow and into the jet. To deal with this problem, two features are added into the second pressure chamber. As the oil-seeded airflow enters the top of the chamber, a set of two baffle plates cause the entering air to make several rapid turns, changing the flow direction rapidly. The larger oil droplets' inertia is so large that they no longer follow the flow and are deposited upon the baffle plates and chamber walls. Exiting the baffle plates the flow proceeds to the bottom of the chamber and the oil collection pool. The jet nozzle is a tubular pipe with an inner diameter of 9.5 mm that extrudes upwards into the pressure chamber for 50 mm. With a diameter of 50 mm for the second chamber, a pooling area is created at the bottom of the chamber for collection of any oil. A pressure tap at the middle of the chamber allows measurement of the differential pressure between the chamber and the atmosphere with a digital manometer. To excite the jet, the rear end of the second chamber is connected to an acoustic resonance box ($18 \times 18 \times 13.5$ in) driven by a 200 W loudspeaker through a 1.5 in. diameter Tygon tube.

The mean velocity at the jet exit without excitation was 4.8 m s^{-1}, and the Reynolds number based on the jet exit diameter was 3020. Without excitation, the exit turbulent intensities at the centre and the shear layer were 5 % and 13.5 %, respectively. A broad power spectrum of velocity fluctuation measured using a hot-wire probe at the exit was observed. The natural free jet without excitation was already turbulent due to the complicated internal structures of the chambers. Then, strong acoustic excitation with a square waveform at 15 Hz was introduced by a loudspeaker powered by an amplifier fed with a square-wave voltage provided by a signal generator. The normalized root mean square (RMS) variation of velocity fluctuation by the mean velocity of the excited jet at the exit was 80 %, indicating that the excited jet was highly unsteady. The distribution of the excitation level at the exit was flat, indicating a planar-wave excitation across the jet.

The axisymmetrical plane of the jet was illuminated by a 2-mm thick laser sheet generated by a Big Sky laser (CFR190) at 15 Hz, and the interval between two
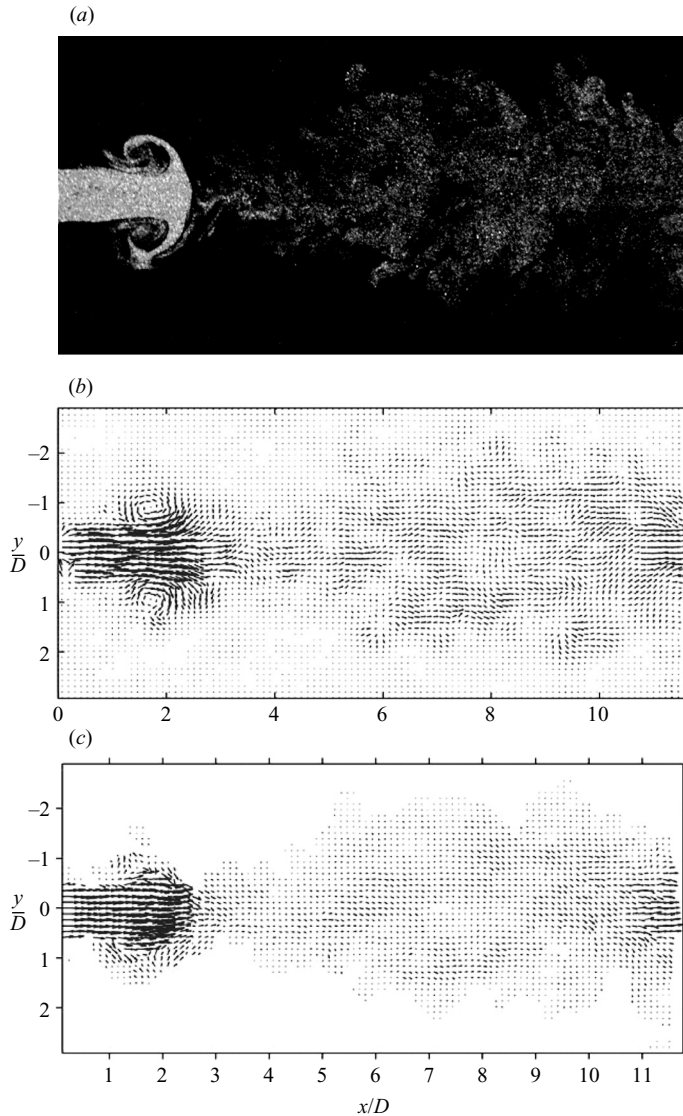
(*a*)

(*b*)

(*c*)

FIGURE 20. (*a*) Typical PIV image of a strongly excited turbulent jet at $T/4$; (*b*) velocity vectors given by the optical flow method; and (*c*) velocity vectors given by the TSI Insight5 PIV software, where $T = 1/15$ s.

pulses was 10 µs. The measuring area was imaged by a PIV camera (TSI PIVCAM 10–30, Model 630046) with an 85 mm lens. Since both the laser and camera were operated at 15 Hz, laser illumination and image acquisition were approximately in phase. Therefore, double-pulsed, snapshot images were obtained in different phases in a period of excitation. Figure 20(*a*) shows a typical PIV image at $T/4$, which is selected from 150 pairs of images in a period of $T = 1/15$ s. The PIV images visualized a vortex ring generated by acoustic excitation and its evolution. To obtain velocity fields, the PIV images were processed using the optical flow algorithm with a Gaussian filter (5×5 pixels mask size and 2 pixels standard deviation) and the TSI Insight5 PIV software (FFT, 32×32 pixels window size). The TSI Insight software

is a typical multi-pass adaptive correlation algorithm that has been comprehensively compared with other PIV algorithms and has had its accuracy documented (Stanislas *et al.* 2005).

Figures 20(*b*) and 20(*c*) show the snapshot velocity fields obtained using the optical flow method and the TSI Insight5 at $T/4$, respectively. The impulse velocity field associated with a vortex ring is also shown. Although the results obtained by the optical flow method are consistent with those given by the correlation method in figure 20, direct comparison of velocity profiles at the same location and same phase is required for quantitative validation. Figure 21 shows the profiles of the x-component of velocity across the jet at different streamwise locations for five phases. It is indicated that the optical flow method and the correlation method (TSI Insight5) give overall consistent results. The relative error $\|u_{1,OP} - u_{1,PIV}\|/\max(u_{1,OP})$ between the results obtained by the optical flow method and the correlation-based method is 3 % in these cases. Near the outer shear layer of the jet, the optical flow method reveals reversed flow induced by a strong vortex ring at some locations. However, this feature is not shown in the profiles given by the TSI Insight5.

Further comparison between the optical flow method and correlation method is made for a temporal variation of the x-component of velocity. Figure 22 shows the temporal variations of the x-component of velocity at $(x/D, y/D) = (1.04, 0)$ and $(x/D, y/D) = (1.04, -0.48)$, where $D = 9.5$ mm is the diameter of the jet exit. At the jet centreline ($y/D = 0$), the optical flow method gives a result consistent with the correlation method. Near the shear layer ($y/D = -0.48$), although the overall shapes and magnitudes of the velocity profiles given by the two methods are close, a large fluctuation (noise) appears in the result given by the TSI Insight5 software.

9. Conclusions

Based on projection of the transport equations or continuity equation onto the image plane, the projected-motion equations are derived for various flow visualizations, and a generic form of these equations is deduced. Further, the physics-based optical flow equation is given, where the optical flow is proportional to the path-averaged velocity of fluid or particles weighted with a relevant field quantity like dye concentration, fluid density and particle concentration. The optical flow is calculated by using the variational method. This work provides a rational foundation for application of the optical flow method to various flow visualization images, including laser-sheet-induced fluorescence images, transmittance images of passive scalar transport, schlieren, shadowgraph and transmittance images of density-varying flows, transmittance and scattering images of particulate flows and laser-sheet-illuminated particle images. The error analysis indicates that the uncertainty of optical flow computation is inversely proportional to the image intensity gradient and directly proportional to the time interval between two successive images. The effects of the image intensity gradient and the time interval on the accuracy of optical flow computation are quantitatively investigated through simulations on synthetic grid images. In principle, the optical flow method is more suitable for images of continuous patterns, providing high-resolution velocity fields. For PIV images, however, it is applicable when particles are sufficiently dense and/or the time interval is small enough and when PIV images are pre-processed by suitable Gaussian filtering. Results consistent with the correlation-based method are obtained by applying the optical flow method to PIV images acquired in a strongly excited turbulent jet. The optical flow method should be further quantitatively examined

FIGURE 21. Profiles of the *x*-component of velocity in a strongly excited turbulent jet obtained by using the optical flow method (lines) and TSI Insight5 PIV software (crosses) at five phases: (*a*) $0T$; (*b*) $T/8$; (*c*) $T/4$; (*d*) $T/2$; and (*e*) $3T/4$, where $T = 1/15$ s.

for various flow visualization images like schlieren and shadowgraph images. The proposed methodology of projecting relevant governing equations onto the image plane is also useful for other image-based measurements.
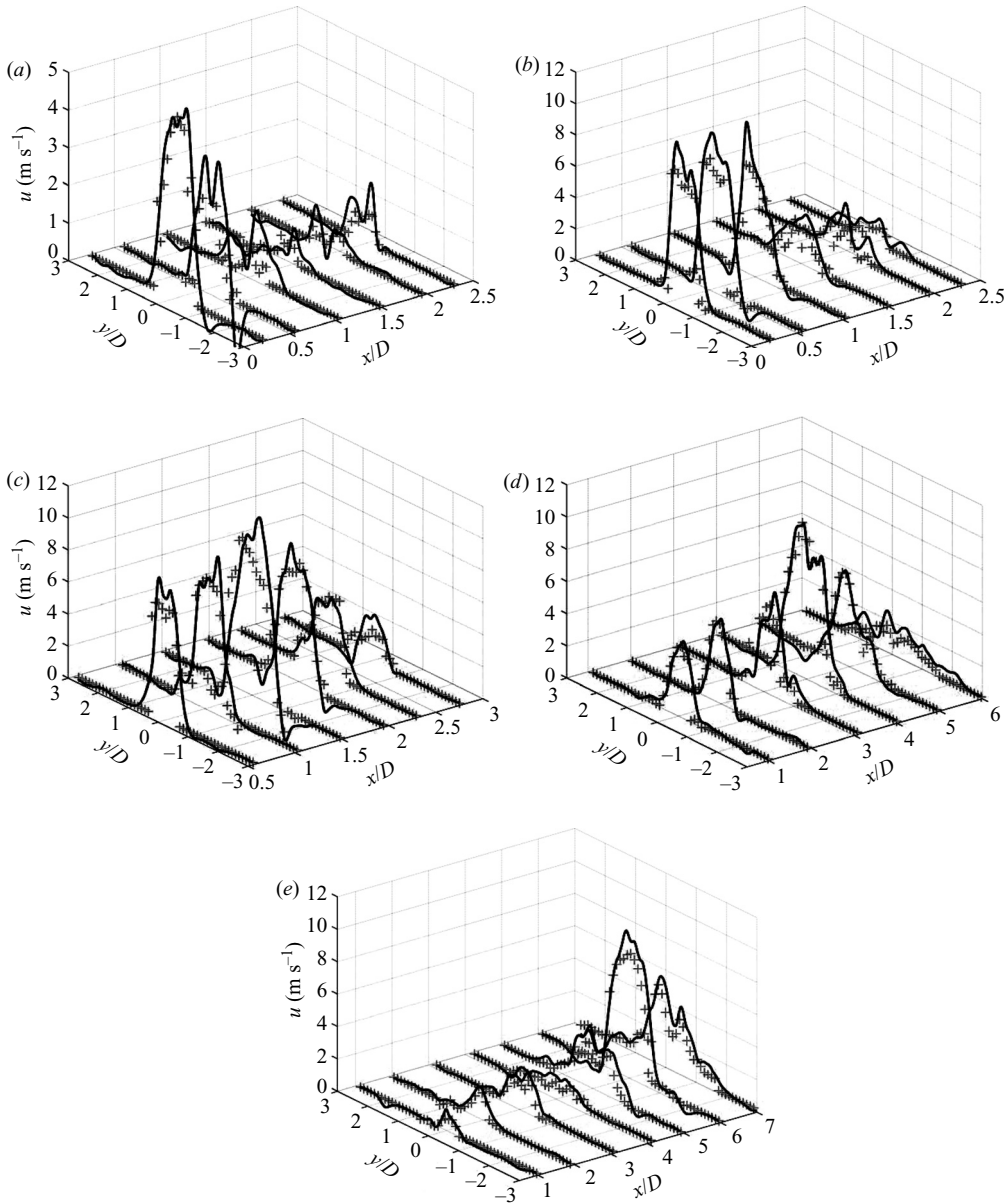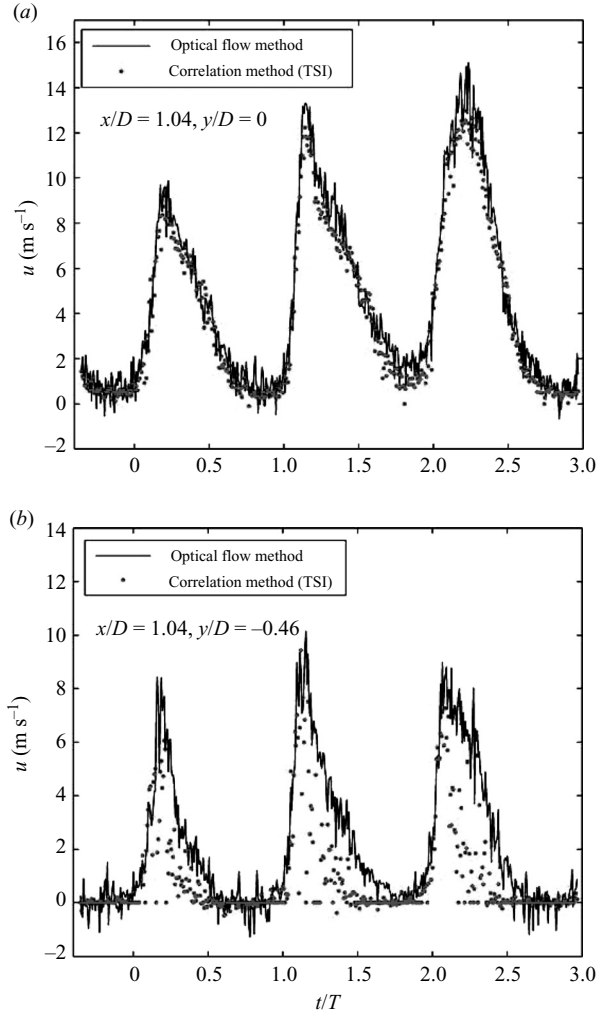
FIGURE 22. Time series of the *x*-component of velocity in a strongly excited turbulent jet obtained by using the optical flow method (lines) and TSI Insight5 PIV software (dots) at (*a*) (*x*/*D*, *y*/*D*) = (1.04, 0) at the jet centreline and (*b*) (*x*/*D*, *y*/*D*) = (1.04, −0.48) in the shear layer.

Appendix A. Derivations of projected-motion equations

A.1. *Laser-sheet-induced fluorescence image*

A.1.1. *Flow with constant fluid density*

A thin laser sheet is often used to illuminate the fluorescent dye seeded in flows for visualization. The fluorescent emission at a certain wavelength is proportional to the dye density, when the dye concentration is sufficiently low. Given a laser-sheet radiance distribution $L_0(X)$ in a three-dimensional space, for a thin laser layer in which the excited dye is optically thin, the fluorescent radiance received by a camera is the integral

$$L(X_1, X_2, t) = c \int_{-\infty}^{\infty} L_0(X)\psi(X, t)\,\mathrm{d}X_3 \approx c L_0(X_1, X_2, X_{3,m}) \int_{\Gamma_1}^{\Gamma_2} \psi(X, t)\,\mathrm{d}X_3, \quad (\mathrm{A}\,1)$$

where $\psi(X, t)$ is the density of the excited molecules; c is a constant; and $X_{3,m}$ is a certain value of X_3 in the laser sheet according to the mean value theorem for integration. Since the distribution of $L_0(X)$ across the laser sheet along X_3 rapidly decays from the laser sheet centre (of which a near-Gaussian distribution can be considered an approximate model), two virtual control surfaces $X_3 = \Gamma_1(X_1, X_2)$ and $X_3 = \Gamma_2(X_1, X_2)$ are placed sufficiently far away from the laser sheet centre that the integral approximation in (A 1) is good. Here, $L_0(X_1, X_2, X_{3,m})$ is interpreted as a mean value of the laser-sheet radiance distribution along X_3, and it is simply denoted by L_0. The laser-sheet radiance for excitation is not uniform due to laser-sheet spreading and dye absorption, and therefore L_0 implicitly depends on the dye density. For a heavily dyed fluid, intensity attenuation in the laser sheet can be measured *a priori* (Dahm & Dimotakis 1987, 1990), and thus L_0 is considered a known distribution in the plane (X_1, X_2).

The transport equation for the concentration of the scalar ψ is

$$\frac{\partial \psi}{\partial t} + U \cdot \nabla \psi = D\nabla^2 \psi, \tag{A 2}$$

where $U = (U_1, U_2, U_3)$ is the fluid velocity, and D is a diffusion coefficient. Most equations in the following sections are expressed in the frame (m_1, m_2, m_3) associated with a camera, and the differential operators are given in the object-space coordinates $X = (X_1, X_2, X_3)$. For a flow with a constant fluid density (such as liquid flows with a constant temperature and incompressible aerodynamic flow), where $U \cdot \nabla \psi = \nabla \cdot (\psi U)$, differentiating (A 1) with respect to time and using (A 2), we have

$$\frac{\partial L}{\partial t} = cL_0 \int_{\Gamma_1}^{\Gamma_2} [-\nabla \cdot (\psi U) + D\nabla^2 \psi]\, \mathrm{d}X_3. \tag{A 3}$$

Furthermore, we have the following relations:

$$\int_{\Gamma_1}^{\Gamma_2} \nabla \cdot (\psi U)\, \mathrm{d}X_3 = \nabla_{12} \cdot \int_{\Gamma_1}^{\Gamma_2} \psi U_{12}\, \mathrm{d}X_3 - n \cdot (\psi U)|_{\Gamma_1}^{\Gamma_2}, \tag{A 4}$$

and

$$\int_{\Gamma_1}^{\Gamma_2} \frac{\partial^2 \psi}{\partial X_\alpha \partial X_\alpha}\, \mathrm{d}X_3 = \frac{\partial^2}{\partial X_\beta \partial X_\beta} \int_{\Gamma_1}^{\Gamma_2} \psi\, \mathrm{d}X_3 + B \quad (\beta = 1, 2; \alpha = 1, 2, 3) \tag{A 5}$$

where $\nabla_{12} = (\partial/\partial X_1, \partial/\partial X_2)$ is the gradient operator ∇ projected on the coordinate plane (X_1, X_2); $U_{12} = (U_1, U_2)$ is the fluid velocity vector projected onto the plane (X_1, X_2); and $n = (\partial X_3/\partial X_1, \partial X_3/\partial X_2, -1)$ is the normal vector of the control surface. The boundary term B in (A 5) is related to ψ and its derivatives on the control surfaces and the gradients of the control surfaces, i.e.

$$B = -n \cdot \nabla \psi|_{\Gamma_1}^{\Gamma_2} - \nabla_{12} \cdot (\psi|_{\Gamma_2} \nabla_{12} \Gamma_2 + \psi|_{\Gamma_1} \nabla_{12} \Gamma_1).$$

We introduce the path-averaged velocity weighted with the dye concentration ψ:

$$\langle U_{12} \rangle_\psi = \frac{\displaystyle\int_{\Gamma_1}^{\Gamma_2} \psi U_{12}\, \mathrm{d}X_3}{\displaystyle\int_{\Gamma_1}^{\Gamma_2} \psi\, \mathrm{d}X_3}. \tag{A 6}$$

Substitution of (A 1), (A 4), (A 5) and (A 6) into (A 3) yields a projected-motion equation:

$$\frac{\partial g}{\partial t} + \nabla_{12} \cdot (g \langle \boldsymbol{U}_{12} \rangle_\psi) = D \nabla_{12}^2 g + D c B + c \boldsymbol{n} \cdot (\psi \boldsymbol{U})|_{\Gamma_1}^{\Gamma_2}, \tag{A 7}$$

where $g = L/L_0$, and $\nabla_{12}^2 = \partial^2/\partial X_\beta \partial X_\beta$ ($\beta = 1, 2$) is the Laplace operator on the projection plane (X_1, X_2). The boundary terms in (A 7) effectively serve as source terms. The last term on the right-hand side of (A 7) represents the accumulation effect of the dye in the illuminated volume moving across the control surfaces. The quantity g can be expressed as $g = L/L_0 = I/I_0$, since the image intensity is proportional to the projected radiance.

For the planar control surfaces, $X_3 = \Gamma_1 = const.$ and $X_3 = \Gamma_2 = const.$, the gradients $\nabla_{12}\Gamma_1$ and $\nabla_{12}\Gamma_2$ in the boundary term B are zero. In addition, for a laser sheet, $\boldsymbol{n} \cdot \nabla \psi|_{\Gamma_1}^{\Gamma_2}$ can be neglected when ψ is constant or linear across the thin laser sheet. Therefore, for laser-sheet visualization, a reasonable approximation is that the boundary term B vanishes. The flux term $\boldsymbol{n} \cdot (\psi \boldsymbol{U})|_{\Gamma_1}^{\Gamma_2}$ could be zero under certain conditions: At the virtual control surfaces, (*a*) the flow is parallel to the planar control surfaces (or the laser sheet); (*b*) the dye concentration is zero; (*c*) the velocity is zero; and (*d*) the incoming and outgoing fluxes into a laser sheet are equal. (The condition (*d*) is usually assumed in laser-sheet visualization.) Under these conditions, the boundary terms, i.e. the last two terms in the right-hand side of (A 7), can be neglected.

A.1.2. *Flow with variable fluid density*

For a flow with a variable fluid density (such as a compressible aerodynamic flow and a buoyancy-driven flow), where the continuity equation is $\partial \rho / \partial t + \nabla \cdot (\rho \boldsymbol{U}) = 0$, we have $\nabla \cdot \boldsymbol{U} = -\rho^{-1}(\partial \rho / \partial t + \boldsymbol{U} \cdot \nabla \rho)$ and $\boldsymbol{U} \cdot \nabla \psi = \nabla \cdot (\psi \boldsymbol{U}) + \psi(\partial/\partial t + \boldsymbol{U} \cdot \nabla) \ln \rho$. Further, we have

$$\int_{\Gamma_1}^{\Gamma_2} \boldsymbol{U} \cdot \nabla \psi \, dX_3 = c^{-1} \nabla_{12} \cdot [(L/L_0) \langle \boldsymbol{U}_{12} \rangle_\psi] - \boldsymbol{n} \cdot (\psi \boldsymbol{U})|_{\Gamma_1}^{\Gamma_2}$$
$$+ c^{-1}(L/L_0) F(K, \rho, \langle \boldsymbol{U}_{12} \rangle_\psi, \langle U_3 \rangle_\psi).$$

The function F is defined as

$$F(K, \rho, \langle \boldsymbol{U}_{12} \rangle_\psi, \langle U_3 \rangle_\psi) = H^{-1} C_1 \partial K / \partial t + H^{-1} C_2 \langle \boldsymbol{U}_{12} \rangle_\psi \cdot (\nabla_{12} K - \ln \rho|_{\Gamma_2} \nabla_{12}\Gamma_2$$
$$+ \ln \rho|_{\Gamma_1} \nabla_{12}\Gamma_1) + H^{-1} C_3 \langle U_3 \rangle_\psi (\ln \rho|_{\Gamma_2} - \ln \rho|_{\Gamma_1})$$

where H is the width between the control surfaces (e.g. the laser sheet thickness); the quantity K is $K = \int_{\Gamma_1}^{\Gamma_2} \ln \rho \, dX_3$, and the correlation coefficients are defined as

$$C_1 = \frac{H \displaystyle\int_{\Gamma_1}^{\Gamma_2} \psi \partial \ln \rho / \partial t \, dX_3}{\displaystyle\int_{\Gamma_1}^{\Gamma_2} \psi \, dX_3 \int_{\Gamma_1}^{\Gamma_2} \partial \ln \rho / \partial t \, dX_3},$$

$$C_2 = \frac{H \displaystyle\int_{\Gamma_1}^{\Gamma_2} \psi \boldsymbol{U}_{12} \cdot \nabla_{12} \ln \rho \, dX_3}{\displaystyle\int_{\Gamma_1}^{\Gamma_2} \psi \boldsymbol{U}_{12} \, dX_3 \cdot \int_{\Gamma_1}^{\Gamma_2} \nabla_{12} \ln \rho \, dX_3},$$

$$C_3 = \frac{H \int_{\Gamma_1}^{\Gamma_2} \psi U_3 \partial \ln \rho / \partial X_3 \, dX_3}{\int_{\Gamma_1}^{\Gamma_2} \psi U_3 \, dX_3 \int_{\Gamma_1}^{\Gamma_2} \partial \ln \rho / \partial X_3 \, dX_3}.$$

Using (A 5) and (A 2), we obtain a projected-motion equation for a flow with a variable fluid density:

$$\frac{\partial g}{\partial t} + \nabla_{12} \cdot (g \langle U_{12} \rangle_\psi) = D \nabla_{12}^2 g + DcB + c\boldsymbol{n} \cdot (\psi \boldsymbol{U})|_{\Gamma_1}^{\Gamma_2} - gF(K, \rho, \langle U_{12} \rangle_\psi, \langle U_3 \rangle_\psi), \quad \text{(A 8)}$$

where $g = L/L_0 = I/I_0$. When the control surfaces are $X_3 = \Gamma_1 = const.$ and $X_3 = \Gamma_2 = const.$, the image plane is parallel to the laser sheet. Furthermore, the laser sheet is so thin that the fluid density ρ is approximately the same between Γ_1 and Γ_2, and thus $K \approx H \ln \rho$. In this case, (A8) becomes

$$\frac{\partial g}{\partial t} + \nabla_{12} \cdot (g \langle U_{12} \rangle_\psi) = D \nabla_{12}^2 g + DcB + c\boldsymbol{n} \cdot (\psi \boldsymbol{U})|_{\Gamma_1}^{\Gamma_2}$$
$$- \rho^{-1} g \left(C_1 \frac{\partial \rho}{\partial t} + C_2 \langle U_{12} \rangle_\psi \cdot \nabla_{12} \rho \right). \quad \text{(A 9)}$$

The effect of the fluid density variation on the projected-motion equation is clearly seen in (A 8) and (A 9), and for a flow with a constant fluid density (A 8) and (A 9) naturally reduce to (A 7).

A.2. *Transmittance image through passive scalar*

When a light ray transmits through passive scalar, the intensity of light at a certain wavelength is attenuated due to absorption and scattering by the scalar. It is assumed that absorption and scattering by fluid are negligible, and the scalar does not change the density of fluid. The radiance reaching a camera through the scalar is

$$L(X_1, X_2, t) = L_0(X_1, X_2) \exp \left(- \int_{\Gamma_1}^{\Gamma_2} \beta(\boldsymbol{X}, t) \, dX_3 \right), \quad \text{(A 10)}$$

where β is the extinction coefficient, and L_0 is the incident radiance. We consider passive scalar confined by the control surfaces $X_3 = \Gamma_1(X_1, X_2)$ and $X_3 = \Gamma_2(X_1, X_2)$ outside which the scalar concentration is zero. The extinction coefficient is proportional to the scalar concentration for sufficiently weak concentration, i.e. $\beta = \varepsilon \psi$, where ε is a coefficient. Since $-\ln(L/L_0)$ from (A 10) has the same form as (A 1), we directly have

$$\frac{\partial g}{\partial t} + \nabla_{12} \cdot (g \langle U_{12} \rangle_\psi) = D \nabla_{12}^2 g - D\varepsilon B - \varepsilon \boldsymbol{n} \cdot (\psi \boldsymbol{U})|_{\Gamma_1}^{\Gamma_2}, \quad \text{(A 11)}$$

where $g = \ln(L/L_0) = \ln(I/I_0)$. When the scalar concentration is small, the radiance can be written as $L = L_0 - \Delta L$, where ΔL is the difference between the incident radiance and detected radiance due to the absorption of a light through the scalar. For $\Delta L/L_0 \ll 1$ and $\Delta L > 0$, so that $\ln(L/L_0) \approx -\Delta L/L_0 = -\Delta I/I_0$, (A 11) becomes

$$\frac{\partial g}{\partial t} + \nabla_{12} \cdot (g \langle U_{12} \rangle_\psi) = D \nabla_{12}^2 g + D\varepsilon B + \varepsilon \boldsymbol{n} \cdot (\psi \boldsymbol{U})|_{\Gamma_1}^{\Gamma_2}, \quad \text{(A 12)}$$

where $g = \Delta L/L_0 = \Delta I/I_0$, and ΔI and I_0 are the image intensity responses to ΔL and L_0, respectively. For the solid control surfaces where $\boldsymbol{n} \cdot (\psi \boldsymbol{U})|_{\Gamma_1}^{\Gamma_2} = 0$ or the virtual control surfaces that are placed sufficiently far away that $\boldsymbol{U} = 0$ and $\psi = 0$, the boundary terms in (A 11) and (A 12) are zero.

A.3. *Images of density-varying flow*

Settles (2001) briefly discussed schlieren image correlation velocimetry. More details of image correlation velocimetry for the determination of a velocity field of continuous patterns were given by Tokumaru & Dimotakis (1995). The projected-motion equations in this paper are derived for the optical flow method to extract velocity fields from schlieren, shadowgraph and transmittance images of density-varying flows.

A.3.1. *Schlieren image*

The schlieren technique has been widely used for flow visualization of density-varying flows such as compressible aerodynamic flows and natural convection flows. The coordinate system is set at the centre of the test section, in which X_2 is in the mean flow direction, and X_3 is in the direction normal to the window walls along a light ray. The control surfaces are given by $X_3 = \Gamma_1(X_1, X_2)$ and $X_3 = \Gamma_2(X_1, X_2)$ through which a light ray passes. The image intensity I in a schlieren image depends on the gradient of the fluid density ρ (Goldstein & Kuehn 1996) by the following relation:

$$\frac{I - I_K}{I_K} = C \int_{\Gamma_1}^{\Gamma_2} \frac{\partial \rho}{\partial X_2}\, \mathrm{d}X_3, \tag{A 13}$$

where I_K is the reference image intensity with the knife edge inserted in the focal plane when no variation of the density exists in the test section, and C is a coefficient related to the setting of a schlieren system. The knife edge is set to be normal to the gradient of the fluid density $\partial \rho / \partial X_2$.

Taking partial differentiation with respect to time in (A 13) and using the continuity equation $\partial \rho / \partial t + \nabla \cdot (\rho \boldsymbol{U}) = 0$, we have

$$-\frac{\partial (I/I_K - 1)}{\partial t} = C \int_{\Gamma_1}^{\Gamma_2} \frac{\partial}{\partial X_2} [\nabla \cdot (\rho \boldsymbol{U})]\, \mathrm{d}X_3. \tag{A 14}$$

The fundamental theory of calculus leads to

$$\int_{\Gamma_1}^{\Gamma_2} \frac{\partial}{\partial X_2} [\nabla \cdot (\rho \boldsymbol{U})]\, \mathrm{d}X_3 = \frac{\partial}{\partial X_2} \int_{\Gamma_1}^{\Gamma_2} \nabla \cdot (\rho \boldsymbol{U})\, \mathrm{d}X_3 - \nabla \cdot (\rho \boldsymbol{U}) \frac{\partial X_3}{\partial X_2} \bigg|_{X_3 = \Gamma_1}^{X_3 = \Gamma_2}.$$

The integral in the first term on the right-hand side of the above relation can be decomposed into

$$\int_{\Gamma_1}^{\Gamma_2} \nabla \cdot (\rho \boldsymbol{U})\, \mathrm{d}X_3 = \nabla_{12} \cdot \int_{\Gamma_1}^{\Gamma_2} \rho \boldsymbol{U}_{12}\, \mathrm{d}X_3 - \boldsymbol{n} \cdot (\rho \boldsymbol{U})|_{\Gamma_1}^{\Gamma_2}.$$

From (A 13), we have

$$\frac{I - I_K}{C I_K} = \frac{\partial}{\partial X_2} \int_{\Gamma_1}^{\Gamma_2} \rho\, \mathrm{d}X_3 - \rho \frac{\partial X_3}{\partial X_2} \bigg|_{X_3 = \Gamma_1}^{X_3 = \Gamma_2},$$

and further

$$\int_{\Gamma_1}^{\Gamma_2} \rho\, \mathrm{d}X_3 = \frac{1}{C} \int_{X_{20}}^{X_2} (I/I_K - 1)\, \mathrm{d}X_2 + \int_{X_{20}}^{X_2} \rho \frac{\partial X_3}{\partial X_2} \bigg|_{X_3 = \Gamma_1}^{X_3 = \Gamma_2}\, \mathrm{d}X_2 + \int_{\Gamma_1}^{\Gamma_2} \rho\, \mathrm{d}X_3|_{X_2 = X_{20}},$$

where X_{20} is a reference position in X_2. The path-averaged velocity weighted with the fluid density ρ can be defined as

$$\langle \boldsymbol{U}_{12} \rangle_\rho = \frac{\int_{\Gamma_1}^{\Gamma_2} \rho \boldsymbol{U}_{12}\, \mathrm{d}X_3}{\int_{\Gamma_1}^{\Gamma_2} \rho\, \mathrm{d}X_3}. \tag{A 15}$$

Substituting the above relations into (A 14), we obtain a projected-motion equation

$$\frac{\partial g}{\partial t} + \boldsymbol{\nabla}_{12} \cdot (g \langle \boldsymbol{U}_{12} \rangle_\rho) = f, \tag{A 16}$$

where

$$g = \int_{X_{20}}^{X_2} (I/I_K - 1)\, \mathrm{d}X_2 + C \int_{\Gamma_1}^{\Gamma_2} \rho\, \mathrm{d}X_3 |_{X_2 = X_{20}},$$

and

$$f = C \frac{\partial}{\partial t} \int_{\Gamma_1}^{\Gamma_2} \rho\, \mathrm{d}X_3 \bigg|_{X_2 = X_{20}} + [\boldsymbol{\nabla}_{12} \cdot (g \langle \boldsymbol{U}_{12} \rangle_\rho)]_{X_2 = X_{20}} + C \left[\boldsymbol{n} \cdot (\rho \boldsymbol{U}) |_{\Gamma_1}^{\Gamma_2} \right]_{X_2 = X_{20}}^{X_2}.$$

The flux term in f vanishes for solid planar control surfaces (like glass windows), and $X_3 = \Gamma_1 = const.$ and $X_3 = \Gamma_2 = const.$ where the no-flux condition $\boldsymbol{n} \cdot (\rho \boldsymbol{U}) = 0$ is imposed. In some applications such as schlieren imaging of buoyancy-driven flow in an open space and focused schlieren imaging, the virtual control surfaces can be placed sufficiently far away from a measurement domain that either the local velocity vanishes ($\boldsymbol{U} = 0$) or the local velocity is parallel to the control surfaces $[\boldsymbol{n} \cdot (\rho \boldsymbol{U}) = 0]$. In this case, the flux term also vanishes. The other terms are related to the values of the flow properties at the reference position $X_2 = X_{20}$. When the reference position is in the incoming free stream in which the fluid density and velocity are steady and spatially uniform, these terms can be neglected.

A.3.2. *Shadowgraph image*

In contrast to a schlieren image, the image intensity I in a shadowgraph image depends on the second-order derivative of the fluid density ρ (Goldstein & Kuehn 1996), i.e.

$$\frac{I - I_T}{I_T} = C \int_{\Gamma_1}^{\Gamma_2} \nabla_{12}^2 \rho\, \mathrm{d}X_3, \tag{A 17}$$

where I_T is the initial image intensity; C is a coefficient related to the setting of a shadowgraph system; and $\nabla_{12}^2 = \partial^2/\partial X_1^2 + \partial^2/\partial X_2^2$. When the control surfaces are planar, i.e. $X_3 = \Gamma_1 = const.$ and $X_3 = \Gamma_2 = const.$, taking partial differentiation with respect to time in (A 17) and using the continuity equation $\partial \rho / \partial t + \boldsymbol{\nabla} \cdot (\rho \boldsymbol{U}) = 0$, we have

$$-\frac{1}{C} \frac{\partial (I/I_T - 1)}{\partial t} = \nabla_{12}^2 \left[\boldsymbol{\nabla}_{12} \cdot \int_{\Gamma_1}^{\Gamma_2} \rho \boldsymbol{U}_{12}\, \mathrm{d}X_3 \right]. \tag{A 18}$$

From (A 17), we have a Poisson equation for the integral of the fluid density:

$$\nabla_{12}^2 \int_{\Gamma_1}^{\Gamma_2} \rho\, \mathrm{d}X_3 = C^{-1}(I/I_T - 1).$$

The integral of the fluid density can be obtained by solving the Poisson equation $\nabla_{12}^2 g = I/I_T - 1$ with suitable boundary conditions. Thus, a projected-motion equation

is symbolically expressed as

$$\frac{\partial g}{\partial t} + \nabla_{12} \cdot (g \langle \boldsymbol{U}_{12} \rangle_\rho) = C \boldsymbol{n} \cdot (\rho \boldsymbol{U})|_{\Gamma_1}^{\Gamma_2}, \qquad (A\,19)$$

where $g = \nabla_{12}^{-2}(I/I_T - 1)$ is a symbolic solution of the Poisson equation, and ∇_{12}^{-2} is the inverse operator of the Poisson equation. The actual form of the projected-motion equation is more complicated than the symbolic one, since the boundary conditions for the Poisson equation should be naturally and explicitly incorporated into the equation.

A.3.3. *Transmittance image*

For certain imaging systems like a collimated monochromatic X-ray system, the image intensity in a transmittance image depends on the fluid density ρ (Wildes *et al.* 2000):

$$\frac{I - I_T}{I_T} = C \int_{\Gamma_1}^{\Gamma_2} \rho \, \mathrm{d}X_3, \qquad (A\,20)$$

where I_T is the initial image intensity, and C is a coefficient related to the setting of an imaging system. For the planar control surfaces, using the technique described above, we obtain

$$\frac{\partial g}{\partial t} + \nabla_{12} \cdot (g \langle \boldsymbol{U}_{12} \rangle_\rho) = C \boldsymbol{n} \cdot (\rho \boldsymbol{U})|_{\Gamma_1}^{\Gamma_2}, \qquad (A\,21)$$

where $g = I/I_T - 1$.

A.4. *Transmittance image through scattering particulate flow*

There are particulate flows in nature and engineering systems such as pyroclastic flows at volcanic eruptions, cloud motion and smoke motion visualizing air flows in wind tunnels. The disperse phase number equation (Brennen 2005) for particulate flow is:

$$\frac{\partial N}{\partial t} + \nabla \cdot (N \boldsymbol{U}) = 0, \qquad (A\,22)$$

where $\boldsymbol{U} = (U_1, U_2, U_3)$ is the particle velocity. The number of particles per unit total volume, N, is given by the particle distribution function $n_p(a)$ of particles of diameter a, i.e.

$$N = \int_0^\infty n_p(a) \, \mathrm{d}a = \langle n_p \rangle_a.$$

The operator $\langle * \rangle_a$ denotes an integral over the entire range of particle sizes.

The light transmittance/scattering through particles depends on the particle distribution. There are three coefficients that generally describe particle scattering and absorption properties. The particle scattering coefficient is defined as

$$\sigma = \int_0^\infty C_{sca} n_p(a) \, \mathrm{d}a = w_{sca} \langle C_{sca} \rangle_a N,$$

where C_{sca} is the scattering cross-section, and w_{sca} is a correlation coefficient. Similarly, the absorption and extinction coefficients of particles are respectively given by

$$\kappa = \int_0^\infty C_{abs} n_p(a) \, \mathrm{d}a = w_{abs} \langle C_{abs} \rangle_a N,$$

and

$$\beta = \int_0^\infty C_{ext} n_p(a)\,\mathrm{d}a = w_{ext}\langle C_{ext}\rangle_a N,$$

where C_{abs} and C_{ext} are the absorption and extinction cross-sections, respectively, and w_{abs} and w_{ext} are the corresponding correlation coefficients.

In the transmittance of a light ray through scattering particulate flow, a portion of light transmits through the medium, and some light is absorbed and scattered by particles. For a one-dimensional plane medium, the equation of radiative transfer for the radiance L in the particulate medium along a ray defined by the unit vector s (or polar angle θ) (Pomraning 1973; Modest 1993) is:

$$\frac{\mathrm{d}L}{\mathrm{d}\tau} + L = S(\tau, s), \tag{A 23}$$

where the source function $S(\tau, s)$ is

$$S(\tau, s) = (1 - \omega)L_b + \frac{\omega}{4\pi}\int_{4\pi} L(s_i)\Phi(s_i, s)\,\mathrm{d}\Omega_i,$$

and the optical coordinate along a ray is $\tau = \int_0^s \beta\,\mathrm{d}s$.

The integral over the solid angle of 4π in this relation represents the gain of radiative energy by the beam due to the radiation incident on the particles from all directions in the spherical space that is scattered by the particles. The scattering phase function $\Phi(s_i, s)$, which gives a directional distribution, represents the probability that the incident radiation along the direction s_i will be scattered into a certain other direction s. Here L_b is the blackbody emission intensity. The single scattering albedo is

$$\omega = \frac{\sigma}{\beta} = \frac{\sigma}{\sigma + \kappa} = \frac{w_{sca}\langle C_{sca}\rangle_a}{w_{ext}\langle C_{ext}\rangle_a},$$

which is independent of the number of particles.

The formal solution of (A 23) gives an integral equation:

$$L(\tau) = L_0\exp(-\tau) + \int_0^\tau S(\tau', s)\exp[-(\tau - \tau')]\,\mathrm{d}\tau'. \tag{A 24}$$

For the fixed-point form of (A 24), given an initial solution $L^{(0)}(\tau)$, the Picard iteration approximation can be used; i.e.

$$L^{(n+1)}(\tau) = L_0\exp(-\tau) + \int_0^\tau S^{(n)}(\tau', s)\exp[-(\tau - \tau')]\,\mathrm{d}\tau', \tag{A 25}$$

where

$$S^{(n)}(\tau, s) = (1 - \omega)L_b + \frac{\omega}{4\pi}\int_{4\pi} L^{(n)}(s_i)\Phi(s_i, s)\,\mathrm{d}\Omega_i.$$

When the Picard iteration converges, we have $L^{(n)}(\tau) \to L(\tau)$ and $S^{(n)}(\tau) \to S^{(\infty)}(\tau)$, as $n \to \infty$. Therefore, the solution to (A 24) can be symbolically written as

$$L(\tau) = L_0\exp(-\tau) + \int_0^\tau S^{(\infty)}(\tau', s)\exp[-(\tau - \tau')]\,\mathrm{d}\tau'. \tag{A 26}$$

The radiance $L(\tau)$ along a certain direction depends on the time and position in a particulate flow in which the number of particles per unit total volume is governed by (A 22). The source function of isotropic scattering particles can be obtained by solving an integral equation (Modest 1993).

We consider the problem in the camera object-space coordinate system (m_1, m_2, m_3). The particulate flow is confined between the control surfaces $X_3 = \Gamma_1(X_1, X_2)$ and $X_3 = \Gamma_2(X_1, X_2)$. The ray direction through the particulate flow to an observer is parallel to the optical axis of a camera (the X_3 axis). The camera (or observer) sees the light through the flow from the opposite side of an illuminating source. In this case, when $\tau = 0$ corresponds to $X_3 = \Gamma_1$ and when τ corresponds to $X_3 = \Gamma_2$, the optical depth is given by

$$\tau_H = \int_{\Gamma_1}^{\Gamma_2} \beta \, dX_3 = w_{ext} \langle C_{ext} \rangle_a \int_{\Gamma_1}^{\Gamma_2} N(t, X) \, dX_3. \qquad (A\,27)$$

The radiance transmitted through the particulate flow is

$$L(\tau_H) = L_0 \exp(-\tau_H) + \int_0^{\tau_H} S^{(\infty)}(\tau', s) \exp[-(\tau_H - \tau')] \, d\tau'. \qquad (A\,28)$$

Differentiation of (A 28) with respect to time and use of (A 28) yield

$$\frac{\partial L(\tau_H)}{\partial t} = w_{ext} \langle C_{ext} \rangle_a \left[S^{(\infty)}(\tau_H) - L(\tau_H) \right] \int_{\Gamma_1}^{\Gamma_2} \frac{\partial N(t, X)}{\partial t} \, dX_3. \qquad (A\,29)$$

Further, using the disperse phase number equation for the particulate flow, we have

$$\int_{\Gamma_1}^{\Gamma_2} \frac{\partial N(t, X)}{\partial t} \, dX_3 = -\int_{\Gamma_1}^{\Gamma_2} \nabla \cdot (NU) \, dX_3 = -\nabla_{12} \cdot \int_{\Gamma_1}^{\Gamma_2} NU_{12} \, dX_3 + n \cdot (NU)|_{\Gamma_1}^{\Gamma_2}.$$

Introducing the path-averaged particle velocity in terms of the particle number

$$\langle U_{12} \rangle_N = \frac{\displaystyle\int_{\Gamma_1}^{\Gamma_2} NU_{12} \, dX_3}{\displaystyle\int_{\Gamma_1}^{\Gamma_2} N \, dX_3}, \qquad (A\,30)$$

we have a projected-motion equation relating the radiance to the average particle velocity

$$\frac{\partial L(\tau_H)}{\partial t} + \left[S^{(\infty)}(\tau_H) - L(\tau_H) \right] \nabla_{12} \cdot (\langle U_{12} \rangle_N \tau_H)$$
$$= w_{wxt} \langle C_{ext} \rangle_a \left[S^{(\infty)}(\tau_H) - L(\tau_H) \right] n \cdot (NU)|_{\Gamma_1}^{\Gamma_2}. \qquad (A\,31)$$

Since the optical depth τ_H can be converted to the radiance through (A 28), (A 31) gives a projected-motion equation relating the radiance emitted from the particulate flow to the path-averaged particle velocity. In particular, for an optically thin medium ($\tau_H \ll 1$), using the approximations $\tau_H \approx [L(\tau_H) - L_0]/[S^{(\infty)}(0) - L_0]$ and $L(\tau_H) \approx L_0$, we have

$$\frac{\partial g}{\partial t} + \nabla_{12} \cdot (g \langle U_{12} \rangle_N) = w_{wxt} \langle C_{ext} \rangle_a n \cdot (NU)|_{\Gamma_1}^{\Gamma_2}, \qquad (A\,32)$$

where $g = [L(\tau_H) - L_0]/[S^{(\infty)}(0) - L_0]$. When the particle scattering and blackbody emission are neglected outside the particulate flow ($S^{(\infty)}(0) = 0$), $g = [L_0 - L(\tau_H)]/L_0 = \Delta I/I_0$, where ΔI is the change of the image intensity that corresponds to a difference between the incident radiance and detected radiance associated with light attenuation through the particulate flow, and I_0 corresponds to the light source intensity. For the solid control surfaces at which the zero-flux condition $n \cdot (NU) = 0$

is valid, the boundary terms on the right-hand side of (A 31) and (A 32) vanish. For a flow in an open space such as pyroclastic flow from an erupting volcano, the virtual control surfaces can be placed sufficiently far away from the volcano that $NU = 0$.

A.5. *Scattering image toward incident direction from particulate flow*

The radiance through the particulate flow contains three terms, i.e. $L(\tau, \mu) = Q_0 + Q_{sca} + Q_{bb}$, where $Q_0(\tau, \mu)$, $Q_{sca}(\tau, \mu)$ and Q_{bb} are the contributions from the incident light, particle scattering and blackbody emission, respectively. The expressions for $Q_{sca}(\tau, \mu)$ for collimate and isotropic incident light can be obtained by solving an integral equation (Modest 1993). Without the blackbody emission, when observing the particulate flow in the general direction of the incident light, we only see the scattered light from the moving particles, since $Q_0 = 0$ and $Q_{bb} = 0$. It is assumed that a ray of the scattered light is parallel to the optical axis of the camera. When an observer on the outside of the control surface Γ_1 sees through it to the control surface Γ_2, the radiance scattered back toward the general incident direction is described by

$$\frac{dL^-}{d\tau^-} + L^- = Q_{sca}(\tau^-), \tag{A 33}$$

where the superscript '$-$' denotes the ray scattered back toward the general incident direction (to the observer), and τ^- is the optical coordinate at the control surface Γ_2 directed to Γ_1. The scattering radiance $Q_{sca}(\tau^-)$ in (A 33) is taken at the directional cosine $\mu = 1$. We know the translational relations, $\tau^- = \tau_H - \tau$ and $s^- = H - s$, where τ is the optical coordinate at Γ_1 directed to Γ_2. Here, the ray path coordinate s (or s^-) is parallel to the coordinate X_3. The distance H between Γ_2 and Γ_1 is considered a penetration depth, and the optical depth is

$$\tau_H = \int_{\Gamma_1}^{\Gamma_2} \beta \, ds = \int_{\Gamma_2}^{\Gamma_1} \beta \, ds^-.$$

The solution to (A 33) for the radiance scattered toward the incident direction is

$$L^-(\tau) = L^-(0) \exp(-\tau^-) + \int_0^{\tau^-} Q_{sca}(\tau_H - \tau') \exp[-(\tau^- - \tau')] \, d\tau', \tag{A 34}$$

where $L^-(0) = L^-(\tau^- = 0)$ is the scattered radiance at Γ_2. The radiance scattered through the particulate flow in the depth between the control surfaces onto a camera is

$$L^-(\tau_H) = L^-(0) \exp(-\tau_H) + \int_0^{\tau_H} Q_{sca}(\tau_H - \tau') \exp[-(\tau_H - \tau')] \, d\tau'. \tag{A 35}$$

Differentiating (A 35) with respect to time and using (A 22), the disperse phase number equation, we have

$$\frac{\partial L^-(\tau_H)}{\partial t} + [R(\tau_H) - L^-(\tau_H)] \nabla_{12} \cdot (\langle U_{12} \rangle_N \tau_H)$$
$$= w_{wxt} \langle C_{ext} \rangle_a [R(\tau_H) - L^-(\tau_H)] \boldsymbol{n} \cdot (NU)|_{\Gamma_1}^{\Gamma_2}, \tag{A 36}$$

where

$$R(\tau_H) = Q_{sca}(0) + \int_0^{\tau_H} \left. \frac{\partial Q_{sca}(\tau^-)}{\partial \tau^-} \right|_{\tau_H - \tau'} \exp[-(\tau_H - \tau')] \, d\tau'.$$

The optical depth τ_H can be converted to the radiance $L^-(\tau_H)$ through (A 35). For the light scattered toward the incident direction, (A 36) has the same form as (A 31) for

the transmitted light through the particulate flow. For $\tau_H \ll 1$, using an approximation $\tau_H \approx [L^-(\tau_H) - L^-(0)]/[Q_{sca}(0) - L^-(0)]$, we have

$$\frac{\partial g}{\partial t} + \nabla_{12} \cdot (g \langle U_{12} \rangle_N) = w_{wxt} \langle C_{ext} \rangle_a \boldsymbol{n} \cdot (N U)|_{\Gamma_1}^{\Gamma_2}, \tag{A 37}$$

where

$$g = [L^-(\tau_H) - L^-(0)]/[Q_{sca}(0) - L^-(0)] = \Delta I / I_0,$$

and ΔI and I_0 are the changes of the image intensity that correspond to $L^-(\tau_H) - L^-(0)$ and $Q_{sca}(0) - L^-(0)$, respectively. For $L^-(\tau_H) \gg L^-(0)$, g is approximately the normalized image intensity that directly responds to the scattered radiance. For many applications where the blackbody emission is important such as satellite infrared imaging, these derivations and results are still valid if Q_{sca} is replaced by $Q_{sca} + Q_{bb}$.

A.6. *Laser-sheet-illuminated particle image*

In typical planar PIV measurements, a thin laser sheet is used to illuminate particles seeded in flows, which is viewed by a camera perpendicularly. The particles illuminated by the laser sheet are between the virtual control surfaces Γ_1 and Γ_2. Based on the similar treatment for laser-sheet-induced fluorescence, the scattering from the particles is proportional to an integral of the number of particles per volume across the laser sheet, i.e.

$$L(X_1, X_2, t) = C L_0(X_1, X_2, X_{3,m}) \int_{\Gamma_1}^{\Gamma_2} N(\boldsymbol{X}, t) \, \mathrm{d}X_3, \tag{A 38}$$

where C is the scattering cross-section, and L_0 is the mean laser-sheet radiance distribution that is known after intensity attenuation due to absorption and scattering has been measured *a priori*. Following the similar procedures described before, we have

$$\frac{\partial g}{\partial t} + \nabla_{12} \cdot (g \langle U_{12} \rangle_N) = C \boldsymbol{n} \cdot (N U)|_{\Gamma_1}^{\Gamma_2}, \tag{A 39}$$

where $g = L/L_0 = I/I_0$, and the path-averaged particle velocity $\langle U_{12} \rangle_N$ is defined by (A 30). The boundary term serving as a source on the right-hand side of (A 39) represents the contribution from particles that move across the laser-sheet boundary surfaces and accumulate within the laser sheet. The particle accumulation in a laser sheet, which is often neglected in planar PIV, has been long recognized as an error source, and its effect on the determination of the velocity field is clearly shown in (A 39).

The radiance projected onto the plane (X_1, X_2) from discrete particles is ideally described by

$$g = \sum_{i=1}^{M} g_i, \tag{A 40}$$

where the radiance from each particle is modelled by the Gaussian distribution

$$g_i = \frac{1}{2\pi \sigma_i^2} \exp\left[-\frac{(X_1 - X_{1,i})^2 + (X_2 - X_{2,i})^2}{2\sigma_i^2} \right].$$

The coordinates $(X_{1,i}, X_{2,i})$ give the centroid location of the ith particle that is a function of time, while the standard deviation σ_i defines its size. Substitution of

(A 40) into (A 39) yields

$$\sum_{i=1}^{M} \frac{g_i}{\eta_i} \left[(X_1 - X_{1,i}) \left(\frac{\mathrm{d}X_{1,i}}{\mathrm{d}t} - \langle U_1 \rangle_N \right) + (X_2 - X_{2,i}) \left(\frac{\mathrm{d}X_{2,i}}{\mathrm{d}t} - \langle U_2 \rangle_N \right) \right.$$

$$\left. + \eta_i \max \left(\sigma_i^2 \right) \boldsymbol{\nabla}_{12} \cdot \langle \boldsymbol{U}_{12} \rangle_N \right] = \max \left(\sigma_i^2 \right) C \boldsymbol{n} \cdot (N \boldsymbol{U}) |_{\Gamma_1}^{\Gamma_2} \qquad (A\,41)$$

where $\eta_i = \sigma_i^2 / \max(\sigma_i^2)$. When $\max(\sigma_i^2) \to 0$ while η_i remains finite, g_i approaches a Dirac delta function, i.e. $g_i \to \delta(X_1 - X_{1,i}, X_2 - X_{2,i})$. In this case, the relation between the velocity of an individual particle and the path-averaged velocity field is

$$(\mathrm{d}X_{1,i}/\mathrm{d}t, \ \mathrm{d}X_{2,i}/\mathrm{d}t) = \delta(X_1 - X_{1,i}, X_2 - X_{2,i}) \langle \boldsymbol{U}_{12} \rangle_N. \qquad (A\,42)$$

A lucid connection between the discrete velocity in PIV/PTV and the continuous path-averaged velocity field is manifested in (A 42) in the differential formulation of the projected-motion equation.

Appendix B. Algorithm

A discrete scheme is given to solve (7), the Euler–Lagrange equation. For simplicity of expression, we denote $\boldsymbol{u} = (u_1, u_2) = (u, v)$ and define

$$(\delta_x u)_{i,j} = (u_{i+1,j} - u_{i-1,j})/2,$$
$$(\delta_y u)_{i,j} = (u_{i,j+1} - u_{i,j-1})/2,$$
$$(\delta_{xy} u)_{i,j} = (u_{i+1,j} - u_{i+1,j-1} - u_{i-1,j+1} + u_{i-1,j-1})/4,$$
$$\bar{u}_{i,j}^x = (u_{i+1,j} + u_{i-1,j}),$$
$$\bar{u}_{i,j} = (u_{i+1,j} + u_{i+1,j-1} + u_{i-1,j+1} + u_{i-1,j-1})/4.$$

Similarly, we can define $(\delta_x v)_{i,j}$, $(\delta_y v)_{i,j}$, $(\delta_{xy} v)_{i,j}$, $\bar{v}_{i,j}^x$ and $\bar{v}_{i,j}$. Using these notations and the 5-point discrete scheme, (7) becomes

$$(gg_{xx} - 2h^{-2}g^2 - 4\alpha h^{-2})u_{i,j} + gg_{xy}v_{i,j}$$
$$= g(f_x - g_{xt}) - g(2g_x(\delta_x u)_{i,j} + g_y(\delta_x v)_{i,j} + g_x(\delta_y v)_{i,j})$$
$$- h^{-2}g^2 \left(\bar{u}_{i,j}^x + (\delta_{xy}v)_{i,j} \right) - \alpha h^{-2} \bar{u}_{i,j}$$
$$gg_{xy}u_{i,j} + (gg_{yy} - 2h^{-2}g^2 - 4\alpha h^{-2})v_{i,j}$$
$$= g(f_y - g_{yt}) - g(2g_y(\delta_x u)_{i,j} + g_x(\delta_y u)_{i,j} + g_y(\delta_y v)_{i,j})$$
$$- h^{-2}g^2 \left((\delta_{xy}u)_{i,j} + \bar{u}_{i,j}^y \right) - \alpha h^{-2} \bar{v}_{i,j},$$

where h is the spatial step that is typically 1 pixel. This linear system is solved by using Jacobi's blockwise iteration method.

REFERENCES

ADRIAN, R. J. 1991 Particle-imaging techniques for experimental fluid mechanics. *Annu. Rev. Fluid Mech.* **23**, 261–304.

AUBERT, G., DERICHE, R. & KORNPROBST, P. 1999 Computing optical flow via variational techniques. *SIAM J. Appl. Maths* **60**(1), 156–182.

BARRON, J. L., FLEET, D. J. & BEAUCHEMIN, S. S. 1994 Performance of optical flow techniques. *Int. J. Comp. Vision* **12**(1), 43–77.

BRENNEN, C. E. 2005 *Fundamentals of Multiphase Flow*, chapter 1. Cambridge University Press.

CORPETTI, T., HEITZ, D., ARROYO, G. & MEMIN, E. 2006 Fluid experimental flow estimation based on an optical flow scheme. *Exps. Fluids* **40**(1), 80–97.

CORPETTI, T., MEMIN, E. & PEREZ, P. 2002 Dense estimation of fluid flows. *IEEE Trans. Patt. Anal. Mach. Intell.* **24**(3), 365–380.

CUZOL, A., HELLIER, P. & MEMIN, E. 2007 A low dimensional fluid motion estimator. *Intl J. Comput. Vision* **75**(3), 329–349.

DAHM, W. J. A. & DIMOTAKIS, P. E. 1987 Measurements of entrainment and mixing in turbulent jets. *AIAA J.* **25**(9), 1216–1223.

DAHM, W. J. A. & DIMOTAKIS, P. E. 1990 Mixing at large Schmidt number in the self-similar far field of turbulent jets. *J. Fluid Mech.* **217**, 299–330.

DAHM, W. J. A., SU, L. K. & SOUTHERLAND, K. B. 1992 A scalar imaging velocimetry technique for fully resolved four-dimensional vector velocity field measurements in turbulent flows. *Phys. Fluids* A **4**(10), 2191–2206.

DRACOS, T. & GRUEN, A. 1998 Videogrammetric methods in velocimetry. *Appl. Mech. Rev.* **51**(6), 387–413.

FAUGERAS, O. & LUONG, Q.-T. 2001 *The Geometry of Multiple Images*, chapter 1. The MIT Press.

FRASER, C. S. 2001 Photogrammetric camera component calibration – A review of analytical techniques. In *Calibration and Orientation of Cameras in Computer Vision* (ed. A. Gruen & T. S. Huang), chapter 4. Springer.

FREDERIKSEN, R. D., DAHM, W. J. A. & DOWLING, D. R. 1997 Experimental assessment of fractal scalar similarity in turbulent flows. Part 2. Higher dimensional intersections and nonfractal inclusions. *J. Fluid Mech.* **338**, 89–126.

GOLDSTEIN, R. J. & KUEHN, T. H. 1996 Optical systems for flow measurement: Shadowgraph, schlieren, and interferometric techniques. In *Fluid Mechanics Measurements*, second edition, (ed. R. J. Goldstein), chapter 7. Taylor & Francis.

GRUEN, A. & HUANG, T. S. 2001 *Calibration and Orientation of Cameras in Computer Vision*. Springer.

HAUSSECKER, H. & FLEET, D. J. 2001 Computing optical flow with physical models of brightness variation. *IEEE Trans. Patt. Anal. Mach. Intell.* **23**(6), 661–673.

HEAS, P., MEMIN, E., PAPADAKIS, N. & SZANTAI, A. 2007 Layered estimation of atmospheric mesoscale dynamics from satellite imagery. *IEEE Trans. Geosci. Remote Sensing* **45**(12), 4087–4104.

HORN, B. K. & SCHUNCK, B. G. 1981 Determining optical flow. *Artif. Intell.* **17**(1–3), 185–204.

KOOCHESFAHANI, M. M. & NOCERA, D. G. 2007 *Molecule Tagging Velocimetry, Handbook of Experimental Fluid Dynamics* (ed. J. Foss, C. Tropea & A. Yarin), chapter 5.4. Springer.

LIU, T. 2004 Geometric and kinematic aspects of image-based measurements of deformable bodies. *AIAA J.* **42**(9), 1910–1920.

LIU, T., CATTAFESTA, L. N., RADEZTSKY, R. H. & BURNER, A. W. 2000 Photogrammetry applied to wind tunnel testing. *AIAA J.* **38**(6), 964–971.

LIU, T., MONTEFORT, J., WOODIGA, S., CONE, K. & SHEN, L. 2008a Mapping skin friction fields in complex flows using luminescent oil. *AIAA Paper* 2008-0267.

LIU, T., MONTEFORT, J., WOODIGA, S., MERATI, P. & SHEN, L. 2008b Global luminescent oil film skin friction meter. *AIAA J.* **46**(2), 476–485.

MAAS, H. G., GRUEN, A. & PAPANTONIOU, D. 1993 Particle tracking velocimetry in three-dimensional flows. *Exps. Fluids* **15**(2), 133–146.

MCGLONE, J. C. 1989 Analytic data-reduction schemes in non-topographic photogrammetry. In *Non-Topographic Photogrammetry*, second edition (ed. H. M. Karara), pp. 37–55. American Society for Photogrammetry and Remote Sensing.

MIKHAIL, E. M., BETHEL, J. S. & MCGLONE, J. C. 2001 *Introduction to Modern Photogrammetry*. John Wiley & Sons.

MITICHE, A. & MANSOURI, A. R. 2004 On convergence of the Horn and Schunck optical-flow estimation method. *IEEE Trans. Image Process.* **13**(6), 848–852.

MODEST, M. F. 1993 *Radiative Heat Transfer*, chapter 8. McGraw-Hill.

POMRANING, G. C. 1973 *The Equations of Radiation Hydrodynamics*. Pergamon.

QUENOT, G. M., PAKLEZA, J. & KOWALEWSKI, T. A. 1998 Particle image velocimetry with optical flow. *Exps. Fluids* **25**, 177–189.

RAFFEL, M., WILLERT, C. & KOMPENHANS, J. 1998 *Particle Image Velocimetry*. Springer.

RUHNAU, P., KOHLBERGER, T., SCHNORR, C. & NOBACH, H. 2005 Variational optical flow estimation for particle image velocimetry. *Exps. Fluids* **38**(1), 21–32.

SETTLES, G. S. 2001 *Schlieren and Shadowgraph Techniques*, chapter 10. Springer.

STANISLAS, M., OKAMOTO, K., KAHLER, C. J. & WESTERWEEL, J. 2005 Main results of the second international PIV challenge. *Exps. Fluids* **39**, 170–191.

SU, L. K. & DAHM, J. A. 1996*a* Scalar imaging velocimetry measurements of the velocity gradient tensor field in turbulent flows, I: Assessment of errors. *Phys. Fluids* **8**(7), 1869–1882.

SU, L. K. & DAHM, J. A. 1996*b* Scalar imaging velocimetry measurements of the velocity gradient tensor field in turbulent flows, II: Experimental results. *Phys. Fluids* **8**(7), 1883–1906.

TIKHONOV, A. N. & ARSENIN, V. Y. 1977 *Solutions of Ill-Posed Problems*, chapter 2. Wiley.

TOKUMARU, P. T. & DIMOTAKIS, P. E. 1995 Image correlation velocimetry. *Exps. Fluids* **19**, 1–15.

TSAI, R. Y. 1987 A versatile camera calibration technique for high-accuracy 3D machine vision metrology using off-the-shelf TV cameras and lenses. *IEEE J. Robot. Automat.* **RA-3**(4), 323–344.

WEICKERT, J. & SCHNORR, C. 2001 A theoretical framework for convex regularization in PDE-based computation of image motion. *Intl J. Comput. Vision* **45**(3), 245–264.

WILDES, R. P., AMABILE, M. J., LANZILLOTTO, A.-M. & LEU, T.-S. 2000 Recovering estimates of fluid flow from image sequence data. *Comp. Vision and Image Understanding* **80**(2), 246–266.

YUAN, J., SCHNORR, C. & MEMIN, E. 2007 Discrete orthogonal decomposition and variational fluid flow estimation. *J. Math. Imaging Vision* **28**(1), 67–80.